

KELT-25b & KELT-26b: A Hot Jupiter and a Substellar Companion Transiting Young A-Stars Observed by *TESS*\*

ROMY RODRÍGUEZ MARTÍNEZ,<sup>1</sup> B. SCOTT GAUDI,<sup>1</sup> JOSEPH E. RODRIGUEZ,<sup>2</sup> GEORGE ZHOU,<sup>2</sup> JONATHAN LABADIE-BARTZ,<sup>3</sup> SAMUEL N. QUINN,<sup>2</sup> KALOYAN PENEV,<sup>4</sup> THIAM-GUAN TAN,<sup>5</sup> DAVID W. LATHAM,<sup>2</sup> LEONARDO A. PAREDES,<sup>6</sup> JOHN F. KIELKOPF,<sup>7</sup> BRETT ADDISON,<sup>8</sup> DUNCAN J. WRIGHT,<sup>8</sup> JOHANNA TESKE,<sup>9</sup> † STEVE B. HOWELL,<sup>10</sup> DAVID CIARDI,<sup>11</sup> CARL ZIEGLER,<sup>12</sup> KEIVAN G. STASSUN,<sup>13,14</sup> MARSHALL C. JOHNSON,<sup>15</sup> JASON D. EASTMAN,<sup>2</sup> ROBERT J. SIVERD,<sup>16</sup> THOMAS G. BEATTY,<sup>17</sup> LUKE BOUMA,<sup>18</sup> TIMOTHY BEDDING,<sup>19</sup> JOSHUA PEPPER,<sup>20</sup> JOSHUA WINN,<sup>18</sup> MICHAEL B. LUND,<sup>11</sup> STEVEN VILLANUEVA JR.,<sup>21, ‡</sup> DANIEL J. STEVENS,<sup>22, 23, §</sup> ERIC L. N. JENSEN,<sup>24</sup> COLEMAN KILBY,<sup>24</sup> JEFFREY D. CRANE,<sup>25, 9</sup> ANDREI TOKOVININ,<sup>26</sup> MARK E. EVERETT,<sup>27</sup> C.G. TINNEY,<sup>28</sup> MICHAEL FAUSNAUGH,<sup>21</sup> DAVID H. COHEN,<sup>24</sup> DANIEL BAYLISS,<sup>29, 30</sup> ALLYSON BIERYLA,<sup>2</sup> PHILLIP A. CARGILE,<sup>2</sup> KAREN A. COLLINS,<sup>2</sup> DENNIS M. CONTI,<sup>31</sup> KNICOLE D. COLÓN,<sup>32</sup> IVAN A. CURTIS,<sup>33</sup> D. L. DEPOY,<sup>34, 35</sup> PHIL EVANS,<sup>36</sup> DAX L. FELIZ,<sup>13</sup> JOAO GREGORIO,<sup>37</sup> JASON ROTHENBERG,<sup>38</sup> DAVID J. JAMES,<sup>2, 39</sup> MICHAEL D. JONER,<sup>40</sup> RUDOLF B. KUHN,<sup>41, 42</sup> MARK MANNER,<sup>43</sup> SOMAYEH KHAKPASH,<sup>20</sup> JENNIFER L. MARSHALL,<sup>34, 35</sup> KIM K. MCLEOD,<sup>44</sup> MATTHEW T. PENNY,<sup>45</sup> PHILLIP A. REED,<sup>46</sup> HOWARD M. RELLES,<sup>2</sup> DENISE C. STEPHENS,<sup>40</sup> CHRIS STOCKDALE,<sup>47</sup> MARK TRUEBLOOD,<sup>48</sup> PAT TRUEBLOOD,<sup>48</sup> XINYU YAO,<sup>20</sup> ROBERTO ZAMBELLI,<sup>49</sup> ROLAND VANDERSPEK,<sup>21</sup> SARA SEAGER,<sup>21, 50, 51</sup> JON M. JENKINS,<sup>10</sup> TODD J. HENRY,<sup>6</sup> HODARI-SADIKI JAMES,<sup>6</sup> WEI-CHUN JAO,<sup>6</sup> SHARON XUESONG WANG,<sup>9</sup> PAUL BUTLER,<sup>25</sup> IAN THOMPSON,<sup>9</sup> STEPHEN SHECTMAN,<sup>9</sup> ROBERT WITTENMYER,<sup>8</sup> BRENDAN P. BOWLER,<sup>52</sup> JONATHAN HORNER,<sup>8</sup> STEPHEN R. KANE,<sup>53</sup> MATTHEW W. MENGEL,<sup>8</sup> TIMOTHY D. MORTON,<sup>54</sup> JACK OKUMURA,<sup>8</sup> PETER PLAVCHAN,<sup>55</sup> HUI ZHANG,<sup>56</sup> NICHOLAS J. SCOTT,<sup>10</sup> RACHEL A. MATSON,<sup>10</sup> ANDREW W. MANN,<sup>57</sup> DIANA DRAGOMIR,<sup>58</sup> MAX GÜNTHER,<sup>21, ¶</sup> ERIC B. TING,<sup>10</sup> ANA GLIDDEN,<sup>21</sup> ELISA V. QUINTANA<sup>32</sup>

<sup>1</sup>Department of Astronomy, The Ohio State University, 140 West 18th Avenue, Columbus, OH 43210, USA

<sup>2</sup>Center for Astrophysics | Harvard & Smithsonian, 60 Garden St, Cambridge, MA 02138, USA

<sup>3</sup>Instituto de Astronomia, Geofísica e Ciências Atmosféricas, Universidade de São Paulo, Rua do Matão 1226, Cidade Universitária, São Paulo, SP 05508-900, Brazil

<sup>4</sup>Department of Physics, The University of Texas at Dallas, 800 West Campbell Road, Richardson, TX 75080-3021 USA

<sup>5</sup>Perth Exoplanet Survey Telescope

<sup>6</sup>Department of Physics and Astronomy, Georgia State University, Atlanta, GA 30302, USA

<sup>7</sup>Department of Physics and Astronomy, University of Louisville, Louisville, KY 40292, USA

<sup>8</sup>University of Southern Queensland, Centre for Astrophysics, West Street, Toowoomba, QLD 4350 Australia

<sup>9</sup>The Observatories of the Carnegie Institution for Science, 813 Santa Barbara St., Pasadena, CA 91101, USA

<sup>10</sup>NASA Ames Research Center, Moffett Field, CA, 94035, USA

<sup>11</sup>Caltech IPAC – NASA Exoplanet Science Institute 1200 E. California Ave, Pasadena, CA 91125, USA

<sup>12</sup>Dunlap Institute for Astronomy and Astrophysics, University of Toronto, Ontario M5S 3H4, Canada

<sup>13</sup>Department of Physics and Astronomy, Vanderbilt University, Nashville, TN 37235, USA

<sup>14</sup>Department of Physics, Fisk University, 1000 17th Avenue North, Nashville, TN 37208, USA

<sup>15</sup>Las Cumbres Observatory, 6740 Cortona Drive, Suite 102, Goleta, CA 93117, USA

<sup>16</sup>Gemini Observatory, Northern Operations Center, 670 N. A'ohoku Place, Hilo, HI 96720, USA

<sup>17</sup>Department of Astronomy and Steward Observatory, University of Arizona, Tucson, AZ 85721, USA

<sup>18</sup>Department of Astrophysical Sciences, Princeton University, 4 Ivy Lane, Princeton, NJ, 08544, USA

<sup>19</sup>School of Physics, Sydney Institute for Astronomy (SIfA), The University of Sydney, NSW 2006, Australia

<sup>20</sup>Department of Physics, Lehigh University, 16 Memorial Drive East, Bethlehem, PA 18015, USA

<sup>21</sup>Department of Physics and Kavli Institute for Astrophysics and Space Research, Massachusetts Institute of Technology, Cambridge, MA 02139, USA

<sup>22</sup>Department of Astronomy & Astrophysics, The Pennsylvania State University, 525 Davey Lab, University Park, PA 16802, USA

<sup>23</sup>Center for Exoplanets and Habitable Worlds, The Pennsylvania State University, 525 Davey Lab, University Park, PA 16802, USA

<sup>24</sup>Department of Physics and Astronomy, Swarthmore College, Swarthmore, PA 19081, USA

<sup>25</sup>Department of Terrestrial Magnetism, Carnegie Institution for Science, 5241 Broad Branch Road, NW, Washington, DC 20015, USA

<sup>26</sup>Cerro Tololo Inter-American Observatory, Casilla 603, La Serena, Chile

<sup>27</sup>National Optical Astronomy Observatory, 950 North Cherry Avenue, Tucson, AZ 85719, USA

<sup>28</sup>Exoplanetary Science at UNSW, School of Physics, UNSW Sydney, NSW 2052, Australia

<sup>29</sup>Department of Physics, University of Warwick, Gibbet Hill Road, Coventry CV4 7AL, UK

Corresponding author: Romy Rodríguez Martínez

rodriguezmartinez.2@buckeyemail.osu.edu

\* This paper includes data gathered with the 6.5 meter Magellan Telescopes located at Las Campanas Observatory, Chile.

<sup>30</sup>Centre for Exoplanets and Habitability, University of Warwick, Gibbet Hill Road, Coventry CV4 7AL, UK

<sup>31</sup>American Association of Variable Star Observers, 49 Bay State Road, Cambridge, MA 02138, USA

<sup>32</sup>Exoplanets and Stellar Astrophysics Laboratory, Code 667, NASA Goddard Space Flight Center, Greenbelt, MD 20771, USA

<sup>33</sup>Ivan Curtis Private Observatory

<sup>34</sup>George P. and Cynthia Woods Mitchell Institute for Fundamental Physics and Astronomy, Texas A&M University, College Station, TX 77843 USA

<sup>35</sup>Department of Physics and Astronomy, Texas A&M university, College Station, TX 77843 USA

<sup>36</sup>El Sauce Observatory, Chile

<sup>37</sup>Atalaia Group & CROW Observatory, Portalegre, Portugal

<sup>38</sup>Department of Physics & Astronomy, University of Wyoming, 1000 E University Ave, Dept 3905, Laramie, WY 82071, USA

<sup>39</sup>Black Hole Initiative at Harvard University, 20 Garden Street, Cambridge, MA 02138, USA

<sup>40</sup>Department of Physics and Astronomy, Brigham Young University, Provo, UT 84602, USA

<sup>41</sup>South African Astronomical Observatory, PO Box 9, Observatory, 7935, Cape Town, South Africa

<sup>42</sup>Southern African Large Telescope, PO Box 9, Observatory, 7935, Cape Town, South Africa

<sup>43</sup>Spot Observatory, Nashville, TN 37206, USA

<sup>44</sup>Department of Astronomy, Wellesley College, Wellesley, MA 02481, USA

<sup>45</sup>Department of Physics and Astronomy, Louisiana State University, Baton Rouge, LA 70803 USA

<sup>46</sup>Department of Physical Sciences, Kutztown University, Kutztown, PA 19530, USA

<sup>47</sup>Hazelwood Observatory, Churchill, Victoria, Australia

<sup>48</sup>Winer Observatory, PO Box 797, Sonoita, AZ 85637, USA

<sup>49</sup>Società Astronomica Lunae, Italy

<sup>50</sup>Department of Earth, Atmospheric and Planetary Sciences, Massachusetts Institute of Technology, Cambridge, MA 02139, USA

<sup>51</sup>Department of Aeronautics and Astronautics, MIT, 77 Massachusetts Avenue, Cambridge, MA 02139, USA

<sup>52</sup>Department of Astronomy, The University of Texas at Austin, Austin, TX 78712, USA

<sup>53</sup>Department of Earth Sciences, University of California, Riverside, CA 92521, USA

<sup>54</sup>Department of Astronomy, University of Florida, 211 Bryant Space Science Center, Gainesville, FL, 32611, USA

<sup>55</sup>George Mason University, 4400 University Drive MS 3F3, Fairfax, VA 22030, USA

<sup>56</sup>School of Astronomy and Space Science, Key Laboratory of Modern Astronomy and Astrophysics in Ministry of Education, Nanjing University, Nanjing 210046, Jiangsu, China

<sup>57</sup>Department of Physics and Astronomy, University of North Carolina at Chapel Hill, Chapel Hill, NC 27599, USA

<sup>58</sup>Department of Physics and Astronomy, University of New Mexico, 1919 Lomas Blvd NE, Albuquerque, NM 87131, USA

## ABSTRACT

We present the discoveries of KELT-25b (TIC 65412605, TOI-626.01) and KELT-26b (TIC 160708862, TOI-1337.01), two transiting companions orbiting relatively bright, early A-stars. The transit signals were initially detected by the KELT survey, and subsequently confirmed by *TESS* photometry. KELT-25b is on a 4.40-day orbit around the  $V = 9.66$  star CD-24 5016 ( $T_{\text{eff}} = 8280^{+440}_{-180}$  K,  $M_{\star} = 2.18^{+0.12}_{-0.11} M_{\odot}$ ), while KELT-26b is on a 3.34-day orbit around the  $V = 9.95$  star HD 134004 ( $T_{\text{eff}} = 8640^{+500}_{-240}$  K,  $M_{\star} = 1.93^{+0.14}_{-0.16} M_{\odot}$ ), which is likely an Am star. We have confirmed the sub-stellar nature of both companions through detailed characterization of each system using ground-based and *TESS* photometry, radial velocity measurements, Doppler Tomography, and high-resolution imaging. For KELT-25, we determine a companion radius of  $R_{\text{p}} = 1.64^{+0.039}_{-0.043} R_{\text{J}}$ , and a 3-sigma upper limit on the companion's mass of  $\sim 64 M_{\text{J}}$ . For KELT-26b, we infer a planetary mass and radius of  $M_{\text{p}} = 1.41^{+0.43}_{-0.51} M_{\text{J}}$  and  $R_{\text{p}} = 1.940^{+0.060}_{-0.058} R_{\text{J}}$ . From Doppler Tomographic observations, we find KELT-26b to reside in a highly misaligned orbit. This conclusion is weakly corroborated by a subtle asymmetry in the transit light curve from the *TESS* data. KELT-25b appears to be in a well-aligned, prograde orbit, and the system is likely a member of a cluster or moving group.

**Keywords:** planetary systems, planets and satellites: detection, stars: individual (KELT-25, KELT-26)

## 1. INTRODUCTION

The field of exoplanets has grown tremendously since the first detection of a transiting exoplanet around a bright star (Charbonneau et al. 2000; Henry et al. 2000) two decades ago. Thousands of planets<sup>1</sup> have been validated orbiting

† NASA Hubble Fellow

‡ Pappalardo Fellow

§ Eberly Fellow

¶ Juan Carlos Torres Fellow

<sup>1</sup> Almost 4100, as of 2019 (<https://exoplanetarchive.ipac.caltech.edu/>)

stars of almost every spectral type, and span a wide range of masses, orbits and likely compositions. Our knowledge of the demographics of short-period giant exoplanets quickly expanded with the advent of dedicated wide-field transit surveys from the ground such as The Hungarian-made Automated Telescope Network (HATNet; Bakos et al. 2007), the HATSouth survey (Bakos et al. 2013), the Wide Angle Search for Planets (WASP/SuperWASP; Pollacco et al. 2006; Collier Cameron et al. 2009), the Qatar Exoplanet Survey (QES; Alsubai et al. 2011), XO (McCullough et al. 2005), the Trans-Atlantic Exoplanet Survey network (TrES; Alonso et al. 2007), and the Kilodegree Extremely Little Telescope (KELT; Pepper et al. 2007, 2012) to mention a few.

The *Kepler* space telescope (Borucki et al. 2010) provided the first statistical survey of a large number of transiting planets over a broad region of radius and orbital period. *Kepler* transformed our understanding of the population of relatively short period ( $P \lesssim 100$  days) planets. Later, the next generation of dedicated wide-field surveys came online, such as the Next Generation Transit Survey (NGTS; Bayliss et al. 2018) and the Multi-site All-Sky CAmERA (MASCARA; Lesage et al. 2014). In addition, based largely on arguments presented in Gould et al. (2003) and Blake et al. (2007), targeted ground-based surveys were initiated such as MEarth (Nutzman & Charbonneau 2008; Charbonneau et al. 2009; Berta et al. 2012), TRAPPIST (Gillon et al. 2017), and SPECULOOS (Delrez et al. 2018), which primarily concentrate their efforts on the search for exoplanets around low-mass stars.

Massive and hot stars are typically avoided by transit surveys because planets around them induce weaker photometric signals (as a result of the lower planet-star radius and mass ratios). More importantly, the host stars have fewer spectral lines, and the lines they do have are significantly broadened by their fast rotation. A large fraction of stars above the Kraft break ( $T_{\text{eff}} \gtrsim 6250\text{K}$ ; Kraft 1967) are observed to rotate significantly faster ( $v \sin I_* \geq 10 \text{ km s}^{-1}$ ) than cooler stars. This is because stars with  $T_{\text{eff}} \gtrsim 6250\text{K}$  have essentially no convective envelopes, and thus do not slow down due to magnetic braking over their evolution. They therefore essentially retain their high primordial spin rates. The relative paucity of spectral features coupled with their faster rotation rates make candidate planetary companions transiting hot stars harder to confirm using the radial velocity method (see e.g., Johnson et al. 2018 and Dholakia et al. 2019). To attempt to circumvent the challenges in searching for planets around massive stars on the main sequence, a number of radial velocity surveys have studied “retired A-stars” – cooler, evolved stars that have moved off the main sequence. Such surveys have yielded a number of discoveries (e.g., Johnson et al. 2007, 2011), but have only been able to sample a relatively small number of target stars due to the focussed nature of radial velocity studies.

Despite the observational challenges posed by hot stars, they provide opportunities to study the most massive, highly-irradiated, close-in planets – in particular the relatively new category of “Ultra Hot Jupiters” (Collier Cameron et al. 2010a). Ultra Hot Jupiters provide a unique opportunity for the detailed atmospheric characterization of highly irradiated giant planets. They have high equilibrium temperatures, allowing one to probe extreme conditions that are not present in the Solar System. In particular, many of these Ultra Hot Jupiters have day-side temperatures that are hot enough to disassociate all molecules, leaving atomic metals as the dominant species on the day side (Gaudi et al. 2017). Furthermore, the exceptionally high day-side temperatures of these planets imply that they are typically close to thermodynamic equilibrium (Kitzmann et al. 2018), making the interpretation of observations much simpler, and resulting in atmospheres that are likely quite different than typical hot Jupiters (Kitzmann et al. 2018; Bell & Cowan 2018; Lothringer et al. 2018). In addition, A-type hosts present opportunities to test the effects of host star mass and binarity, and short evolutionary timescales, on giant planet formation, evolution, and engulfment by their host stars. For example, a recent study found that most giant planets around A-type stars are eventually engulfed by their host stars (Stephan et al. 2018), and a related study determined the observable effects of engulfment (Stephan et al. 2019). In general, the high temperatures and high scale heights of Ultra Hot Jupiters make follow-up observations much easier, allowing one to test models of hot Jupiter atmospheres (e.g., Cauley et al. 2019; Hoeijmakers et al. 2019).

Studying the planetary population of massive (A) stars is also interesting for other reasons. First, the large amount of high-energy radiation they emit helps to test theories of planet atmospheric evaporation. Second, the fact that A stars tend to be rapidly rotating means that they are typically oblate, resulting in significant gravity darkening, which can be used to estimate the true (not just projected) spin-orbit angle of the planet (Barnes 2009). The oblateness of the host star, combined with certain orbital alignments of the planet, can result in relatively short precession times of the planetary orbit (Johnson et al. 2015). Finally, their short lifetimes imply that the lifetimes of close-in planets orbiting such stars is likely to be much shorter than that of such planets orbiting low-mass stars (Stephan et al. 2018).

Royer et al. 2007 found that typical rotational values ( $v \sin I_*$ ) are greater than  $100 \text{ km s}^{-1}$  for stars in the B9-F2 spectral range (for reference, the Sun’s rotational velocity is only  $1.6 \pm 0.3 \text{ km s}^{-1}$ ; Pavlenko et al. 2012). Because of the difficulties in confirming planets orbiting these fast rotators, KELT routinely uses a combination of radial velocity (RV) and Doppler Tomographic (DT) observations (Collier Cameron et al. 2010b). DT measures the distor-

tion in the spectral lines of a star caused by the transiting planet blocking the light from the star with different projected velocities as it crosses the disk of the star. Doppler tomographic observations can help confirm that the planet transits the target star and is not, for example, a signal from a nearby eclipsing binary, although confirming the planetary nature of the occulter also requires an appropriately stringent upper limit on its mass (see, e.g., Bieryla et al. 2015 for a discussion of validating planets orbiting rapidly rotating stars using Doppler Tomography). The advantage of this technique is that it is better suited to faster stellar rotations, thereby providing an alternative way to confirm planets around hot stars. Many discovery papers have demonstrated that A-type stars are the most suitable for the measurement of the Rossiter-McLaughlin (RM) effect because they have the optimal combination of  $R_p/R_s$  and rotation – two parameters to which the RM signal is proportional (see also Gaudi & Winn 2007, and Table 8 of this paper).

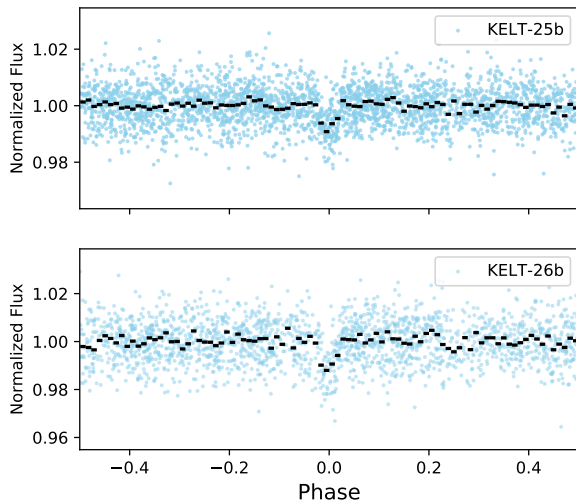


**Figure 1.** Discovery light curves for KELT-25 b (Top) and KELT-26 b (Bottom) from the KELT-South telescope. The light curves are phase-folded on the preliminary orbital periods of 4.401093 days (KELT-25 b) and 3.344886 days (KELT-26 b). The blue points represent the data and the black points are the data binned at intervals of 0.01 in phase.

With Doppler Tomography, we can not only validate new planets, but also determine their projected spin-orbit angles,  $\lambda$ . From the current sample of over 200 systems<sup>2</sup> with measured  $\lambda$ , a dichotomy in stellar temperature has emerged: giant planets around cool stars ( $T_{\text{eff}} < 6200$  K) have lower obliquities than those around hot stars (Schlaufman 2010;

Winn 2010; Dawson et al. 2015). In addition, the most massive planets ( $M_p > 3M_J$ ) tend to have lower spin-orbit angles (Hébrard et al. 2010). These results are important because they help constrain planet formation and migration mechanisms for hot Jupiters. One area of ongoing research is the question of whether hot Jupiters form “in situ” or at larger separations from their host and then migrate into their present observed locations via planet-disk or planet-planet dynamical or secular interactions, or secular interactions with a distant planetary, brown dwarf, or stellar companion (e.g., Dawson & Johnson 2018). Measurements of  $\lambda$  provide insights into these formation channels since different theories predict different values of the distribution of spin-orbit angles.

Giant planets at close separations are highly irradiated by their host stars, and this intense radiation can significantly impact their properties. One possible consequence is radius inflation: it has been observed that hot Jupiters’ radii appear to increase with increasing incident radiation from the host star (Demory & Seager 2011; Howell et al. 2019), although it is not clear whether this is caused by the radiation re-inflating the planet, or because it simply slows the cooling and contraction process of the planets, which may be hot and thus inflated upon formation.

In this paper, we present the discoveries of a sub-stellar companion and likely planet (KELT-25 b) and a hot Jupiter (KELT-26 b<sup>3</sup>) both orbiting bright, early A-stars, first identified as candidates in KELT data and subsequently observed by the *TESS* mission. Although the *TESS* mission’s main science driver is to measure small planets, simulations have estimated yields of thousands of giant planets, which include Jupiter-sized planets around bright stars (e.g. Barclay et al. 2018). *TESS*’s expected yield complements the discoveries made by KELT and other ground-based surveys and advances our understanding of giant planets around hot stars.

## 2. DISCOVERY AND FOLLOW-UP OBSERVATIONS

### 2.1. *KELT* Discovery

One survey that has contributed significantly to the discovery and study of Ultra Hot Jupiters is the Kilodegree Extremely Little Telescope survey (KELT<sup>4</sup>; Pepper et al. 2007). KELT observes  $\sim 85\%$  of the sky targeting bright stars in the magnitude range  $7.5 < V < 12$ , filling in the gap between radial velocity surveys and other transit surveys, which gen-

<sup>3</sup> Whilst we were writing this manuscript, we noted a paper on arXiv in which WASP announced the discovery of WASP-178b (Hellier et al. 2019). We had already collected and analyzed the data needed to confirm KELT-26 b, and other than to confirm that KELT-26 and WASP-178 had the same coordinates, we did not read or use the results of Hellier et al. (2019) in any way. We therefore claim an independent discovery (regardless of whether or not they are the same planet). If they are the same planet, we do not, of course, claim to be the first to have made the detection.

<sup>4</sup> <https://keltsurvey.org>

<sup>2</sup> <https://www.astro.keele.ac.uk/jkt/tepcat/obliquity.html>



**Table 1.** Literature Properties for KELT-25 and KELT-26

Parameter	Description	KELT-25	KELT-26	Source
Other identifiers				
		CD-24 5016	HD 134004	
		TIC 65412605	TIC 160708862	
		TYC 6528-1639-1	TYC 7829-2324-1	
$\alpha_{J2000}$	Right Ascension (RA)	07:12:29.55004	15:09:04.89304	1
$\delta_{J2000}$	Declination (Dec)	-24:57:12.82193	-42:42:17.78910	1
$l$	Galactic Longitude	237.5346109°	328.1938368°	1
$b$	Galactic Latitude	-6.79674034°	+13.3150904°	1
$B_T$	Tycho $B_T$ mag.	9.841±0.019	10.083 ± 0.028	2
$V_T$	Tycho $V_T$ mag.	9.655±0.018	9.961 ± 0.033	2
$G$	Gaia $G$ mag.	9.5960±0.0003	9.912 ± 0.020	1
$J$	2MASS $J$ mag.	9.362 ± 0.03	9.775 ± 0.030	3
$H$	2MASS $H$ mag.	9.273 ± 0.02	9.735 ± 0.020	3
$K_S$	2MASS $K_S$ mag.	9.248 ± 0.02	9.703 ± 0.020	3
$WISE1$	$WISE1$ mag.	9.213 ± 0.022	9.670 ± 0.030	4
$WISE2$	$WISE2$ mag.	9.245 ± 0.02	9.683 ± 0.030	4
$WISE3$	$WISE3$ mag.	9.302 ± 0.033	9.645 ± 0.043	4
$\mu_\alpha$	Gaia DR2 proper motion in RA (mas yr <sup>-1</sup> )	-2.276 ± 0.06	-10.011 ± 0.122	1
$\mu_\delta$	Gaia DR2 proper motion in DEC (mas yr <sup>-1</sup> )	0.338 ± 0.075	-5.652 ± 0.097	1
$\pi^\dagger$	Gaia Parallax (mas)	2.342 ± 0.043 <sup>†</sup>	2.394 ± 0.060 <sup>†</sup>	1
$RV$	Absolute radial velocity (km s <sup>-1</sup> )	35.472±1.011	-24.140 ± 0.045	This work
$d$	Distance (pc)	427.0 ± 7.8	417.7 ± 10.5	1
$U^*$	Space Velocity (km s <sup>-1</sup> )	-13.40 ± 0.58	-24.63 ± 0.37	§5.1
$V$	Space Velocity (km s <sup>-1</sup> )	-13.83 ± 0.84	6.75 ± 0.58	§5.1
$W$	Space Velocity (km s <sup>-1</sup> )	-1.24 ± 0.19	0.78 ± 0.20	§5.1

**NOTES:** <sup>†</sup> Parallaxes here are corrected for the 82  $\mu$ s offset reported in Stassun & Torres (2018a).

\* $U$  is in the direction of the Galactic center.

References: <sup>1</sup>Gaia Collaboration et al. (2018), <sup>2</sup>Høg et al. (2000), <sup>3</sup>Cutri et al. (2003), <sup>4</sup>Zacharias et al. (2017)

erally focus on brighter and fainter stars, respectively. KELT consists of two observatories: KELT-South (KS, Pepper et al. 2012), located in Sutherland, South Africa, which surveys most of the southern hemisphere, and KELT-North (KN), which observes the northern hemisphere from Sonoita, Arizona. KN and KS have been successful at finding giant planets around hot stars, discovering 24 planets, of which 18 – including the ones confirmed in this paper – orbit A and F stars.

Using two separate 42mm-aperture telescopes, the KELT survey observes over 85% of the entire sky with a 20–30 minute cadence. Each observing site has a Mamiya 645 80mm f/1.9 42mm lens with a 4k×4k Apogee CCD on a Paramount ME mount. The KELT telescopes have a 23'' pixel scale and a 26° × 26° field of view. The original goal of the KELT survey was to discover hot Jupiters orbiting bright ( $7 < V[mag] < 12$ ) host stars, which are amenable to detailed characterization through transmission or eclipse

spectroscopy. More recently, KELT has become a significant contributor to the understanding of planets around early-type stars, specifically with the discovery of 6 transiting hot Jupiter around A-stars, including the planets presented here (Zhou et al. 2016; Gaudi et al. 2017; Lund et al. 2017; Johnson et al. 2018; Siverd et al. 2018).

The likely planetary companion orbiting TIC 65412605 (hereafter KELT-25 b) was first identified as a planet candidate following the reduction of KELT-South field KS35. KELT-25 is located at  $\alpha_{J2000} = 07^h 12^m 29^s 55$ ,  $\delta_{J2000} = -24^\circ 57' 12'' 82$  (Gaia Collaboration et al. 2018) and the KELT-South survey field 35 is centered at  $\alpha_{J2000} = 07^h 40^m 12^s 0$ ,  $\delta_{J2000} = -20^\circ 00' 00'' 0$ . KS35 was observed 2,860 times from UT 2013 May 10 until UT 2017 October 1. The image reduction and candidate selection pipeline are described in detail in Siverd et al. (2012) and Kuhn et al. (2016), and are briefly summarized here. To reduce the raw survey images, KELT uses a modified, image subtraction pipeline based on the ISIS software (Alard & Lupton 1998; Alard 2000). The list of sources identified in the KELT fields are then cross-matched to the Tycho-2 (Høg et al. 2000) and UCAC4 (Zacharias et al. 2013) catalogs to obtain their proper motions. We then implement reduced proper motion (RPM) cuts to identify and exclude giants before searching for transit signals (Gould & Morgan 2003; Collier Cameron et al. 2007). Finally, we search for transit-like features in all stars that passed the RPM cuts using the Box-fitting Least Squares (BLS) algorithm (Kovács et al. 2002).

The planet orbiting TIC 160708862 (hereafter KELT-26 b) is located at  $\alpha_{J2000} = 15^h 09^m 04^s 89304$ ,  $\delta_{J2000} = -42^\circ 42' 17'' 78910$  (Gaia Collaboration et al. 2018) in the KELT-South KS37 field, which is centered at  $\alpha_{J2000} = 15^h 07^m 12^s 00$ ,  $\delta_{J2000} -53^\circ 00' 00'' 00$ . This field was observed 2,085 times from UT 2013 September 5 until UT 2015 September 11.

Both companions were identified as candidates from a periodicity search using the BLS algorithm. KELT-25 b was initially identified with a BLS orbital period of 4.40 days and a transit depth of 0.66%, while KELT-26 b was detected with a period of 3.34 days and a 1.1% transit depth. The phase-folded KELT discovery light curves are shown in Figure 1. See Table 1 for literature information about the stellar hosts KELT-25 and KELT-26.

## 2.2. TESS Photometry

The NASA *Transiting Exoplanet Survey Satellite* (TESS, Ricker et al. 2015) was launched on April 18, 2018 with the primary goal of discovering and characterizing small ( $R_p < 4R_\oplus$ ) exoplanets around bright, nearby stars. Presently, dozens of exoplanets have already been validated, while almost a thousand candidates await confirmation. The confirmed systems include a few giant planets on short-period

**Table 2.** Follow-up photometric observations of KELT-25b and KELT-26b

Target	Observatory	Date (UT)	Diameter (m)	Filter	FOV	Pixel Scale	Exposure (s)
KELT-25b	PEST	2019 January 18	0.3	<i>Rc</i>	$31' \times 21'$	$1.2''$	30
KELT-25b	<i>TESS</i>	2019 January 7 - 2019 February 7	0.105	<i>TESS</i> (600-1000nm)	$24^\circ \times 24^\circ$	$21''$	1800
KELT-26b	PEST	2016 August 26	0.3	<i>I</i>	$31' \times 21'$	$1.2''$	30
KELT-26b	Mt. Kent CDK700	2018 March 20	0.6858	<i>r'</i>	$27.3' \times 27.3'$	$0.4''$	65
KELT-26b	<i>TESS</i>	2019 April 22 - 2019 May 20	0.105	<i>TESS</i> (600-1000nm)	$24^\circ \times 24^\circ$	$21''$	1800

orbits (Brahm et al. 2018; Nielsen et al. 2019; Rodriguez et al. 2019a).

KELT-25 was observed in Sector 7 by Camera 2 of the *TESS* spacecraft between UT 2019 January 7 and February 7. We made use of the 30-minute cadence Full Frame Images (FFI) made available by the Mikulski Archive for Space Telescopes (MAST) and calibrated by the Science Processing Operations Center (SPOC) pipeline (Jenkins et al. 2016). Cutouts of  $10 \times 10$  pixels were extracted from the FFIs around each target star via the MAST *TESScut* tool, and aperture photometry was performed using the *lightkurve* package (Lightkurve Collaboration et al. 2018; Barentsen et al. 2019). The target star aperture encompassing pixels around each target star with fluxes higher than 90% of pixels in the cutout, and pixels nearby that do not encompass adjacent stars were used in the evaluation of the background flux. We accounted for dilution within the *TESS* aperture by computing for and removing the light contribution of known nearby stars, as per their *TESS* band magnitudes in TIC.

Similarly, KELT-26 was observed by *TESS* between UT 2019 April 22 and May 20 during Sector 11 of the mission. The light curve extraction for KELT-26 was the same as that described above. Figures 2 and 3 show the raw and reduced *TESS* light curves for KELT-25 b and KELT-26 b.

### 2.3. Ground-based Photometry from the KELT Follow-up Network

In order to confirm that the transit signals are due to bona fide planetary companions, rule out false positives such as eclipsing binaries, and refine the transit depth, duration and ephemeris of our candidates, we obtained photometric observations of KELT-25 b and KELT-26 b from the KELT Follow-Up Network (KELT-FUN, Collins et al. 2018). Some of the follow-up photometry was reduced using the *AstroImageJ* analysis software (Collins et al. 2017). See Table 2 for technical information about the observatories that followed-up these systems. The KELT-FUN transits for both systems are shown in Figures 4 and 5.

**Table 3.** Relative Out-of-Transit Radial Velocities for KELT-25 from TRES

BJD <sub>TDB</sub>	RV (m s <sup>-1</sup> )	$\sigma_{RV}$ (m s <sup>-1</sup> )
2458509.81953	3601.8	384.5
2458511.84309	1657.2	380.6
2458573.61546	480.7	457.1
2458575.63514	991.1	588.0
2458588.63382	1544.3	421.7
2458589.63349	54.5	452.6
2458591.62656	588.2	422.2
2458592.62509	41.9	593.6
2458593.63010	-2782.7	620.8

We note that while the radial velocities have been put on an absolute scale for the CHIRON data, the uncertainties are only relative to the mean. There is an additional systematic uncertainty that would affect all of the data points by the same amount of roughly  $40 \text{ m s}^{-1}$ , due to the uncertainties of the standard radial velocity stars used to put the radial velocities on an absolute scale.

#### 2.3.1. Perth Exoplanet Survey Telescope

The PEST home observatory was built in 2010 and has since helped discover dozens of exoplanets, including KELT candidates, mostly via the transit method. It is located in Perth, Australia, and is owned and run by Thiam-Guan Tan. The instrument is a 0.3m Meade LX200 SCT f/10 and focal reducer yielding f/5. The camera is a SBIG ST-8XME with multiple filters including *I*, and it has a FOV of  $31' \times 21'$  and an image scale of  $1.2''$  per pixel. PEST observed a full transit of KELT-25 b on UT 2019 January 18 and a full transit of KELT-26 b in the *I* filter on UT 2016 July 26.

#### 2.3.2. Mt Kent CDK700 Telescope

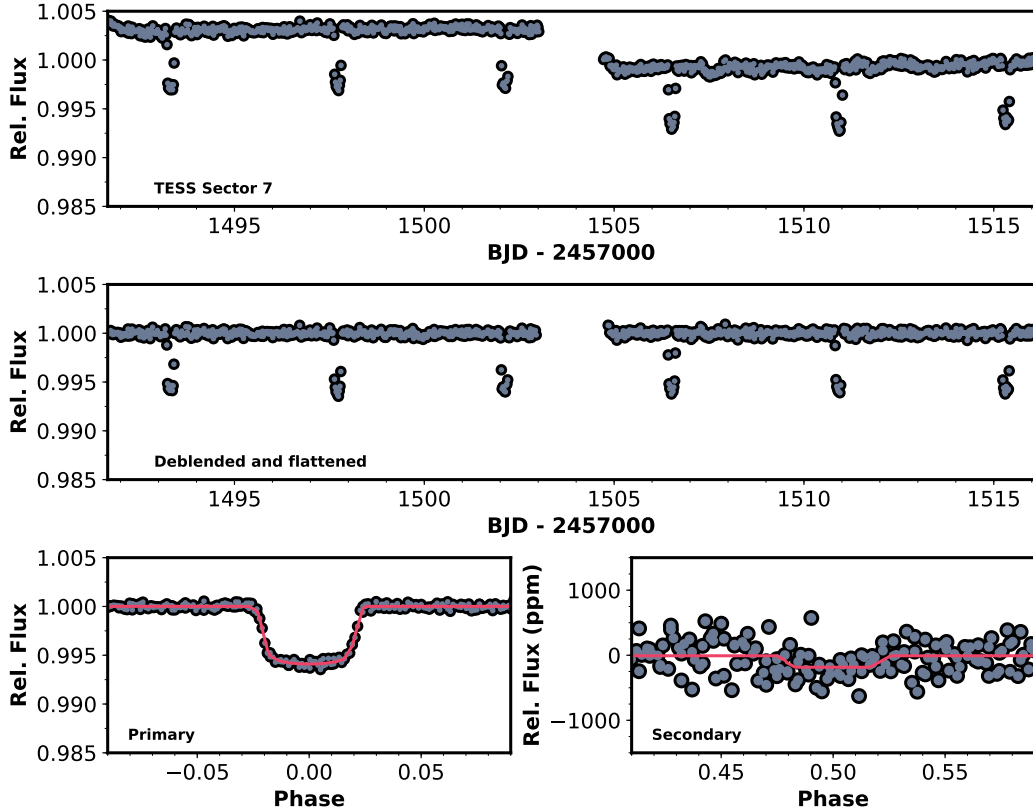


**Figure 2.** *TESS* light curve of KELT-25. The **Top** panel shows the raw light curve; the **middle** panel shows the detrended light curve. The Bottom **Left** panel shows the transit and best-fit EXOFASTv2 model to the detrended light curve, phase-folded on the orbital period. The Bottom **Right** plot shows the region of the secondary eclipse, which is clearly detected in *TESS*.

**Table 4.** Relative Out-of-Transit Radial Velocities for KELT-26 from CHIRON

BJD <sub>TDB</sub>	RV (m s <sup>-1</sup> )	$\sigma_{RV}$ (m s <sup>-1</sup> )
2458527.84082	132.1	54.9
2458532.82920	-112.1	75.8
2458578.72286	182.9	78.3
2458579.85037	-39.4	53.0
2458580.80996	-124	55.3
2458581.79719	68.9	45.5
2458582.83253	-110.5	69.3
2458583.76093	-89	75.3
2458596.78738	-131.7	59.3
2458625.76755	175.2	56.7
2458635.75959	115.8	97.9
2458636.64304	-72.5	72.2
2458637.66033	9.7	56.1
2458639.66539	-120.3	46.8
2458649.51090	233.2	178.2

Photometric follow-up of KELT-26 was taken with the University of Louisville’s Shared Skies MKO-CDK700 telescope at Mt. Kent Observatory of the University of Southern Queensland, Australia. The instrument is a 0.7m Planewave corrected Dall-Kirkham (CDK) telescope with a Nasmyth focus. The telescope was used with an Apogee U16 CCD camera (Kodak KAF-16801E sensor). The CDK700 telescope observed a full transit of KELT-26b, acquiring 165 images in the Sloan  $r'$  filter on UT 2018 March 20.

### 3. SPECTROSCOPIC OBSERVATIONS

#### 3.1. *TRES* Spectroscopy of KELT-25

To constrain the planet mass and characterize the host star properties of KELT-25, we made a series of spectroscopic observations with the Tillinghast Reflector Echelle Spectrograph (TRES; Fűrész 2008) on the 1.5 m telescope at the Fred Lawrence Whipple Observatory (FLWO) in Arizona, USA. TRES is a fiber-fed echelle spectrograph with a resolving power of  $\lambda/\Delta\lambda \equiv R = 44,000$  spanning 3850–9100 Å. A series of spectra were obtained for KELT-25 over 10 epochs from UT 2019 January 26 to UT 2019 May 20. These observations are reduced via the procedure described in Buch-

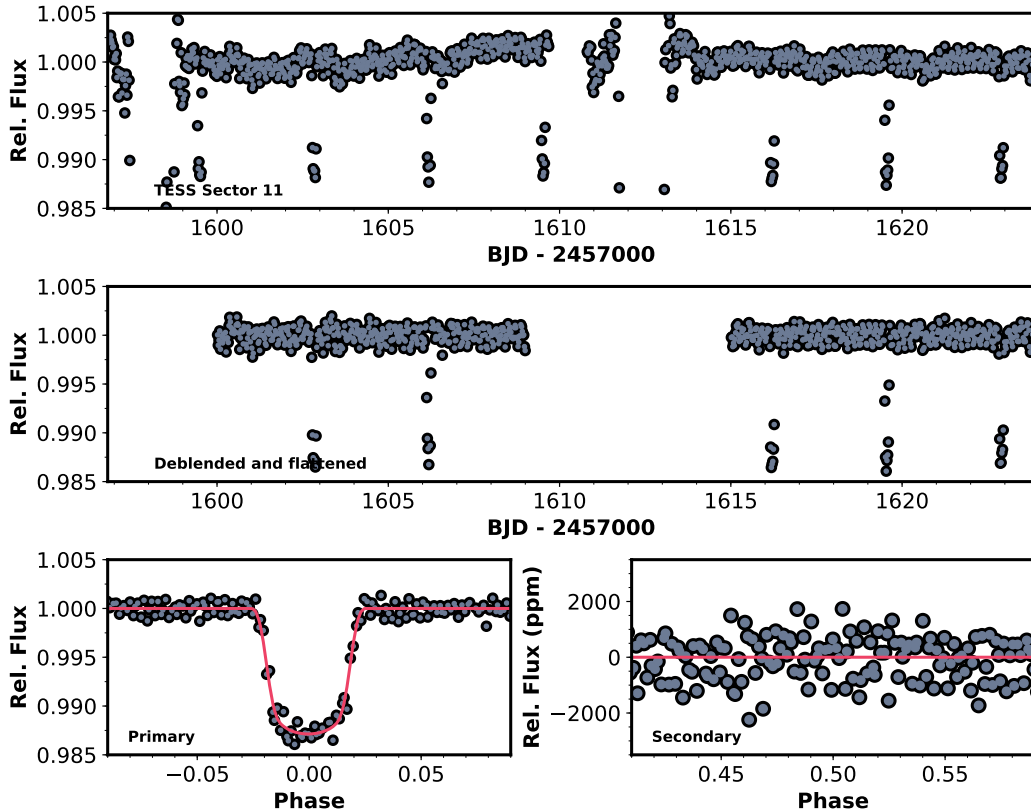


**Figure 3.** *TESS* light curve of KELT-26. The **Top** panel shows the raw light curve; the **middle** panel shows the detrended light curve. The Bottom **Left** panel shows the transit and best-fit EXOFASTv2 model to the detrended light curve, phase-folded on the orbital period. The Bottom **Right** plot shows the region of the secondary eclipse. While the secondary eclipse is not detected in the *TESS* data, the primary phase-folded transit shows evidence for a slight asymmetry, which is likely real and may be caused by gravity darkening of the star. However, the primary also shows periodic photometric oscillations at a period that is nearly commensurate (1:18) with the period of the planet. This variability may also be causing the slight asymmetry.

have et al. (2012), and relative velocities were obtained via a multi-order cross correlation against an averaged observed spectral template, as per Quinn et al. (2012). The relative velocities are listed in Table 3 and plotted in Figure 6.

To establish the absolute systemic velocity of the system, we cross correlated the Mg b line order of one of the observed spectra against a synthetic template, and shifted all other velocities relative to this template.

### 3.2. CHIRON Spectroscopy of KELT-25 and KELT-26

We obtained a series of spectroscopic observations of KELT-25 and KELT-26 with the CHIRON spectrograph on the SMARTS 1.5 m telescope, located at Cerro Tololo Inter-American Observatory (CTIO), Chile. CHIRON is a fiber-fed echelle spectrograph, sliced via an image slicer, yielding a resolving power of  $R = 80,000$  over the wavelength range 4100–8700 Å (Tokovinin et al. 2013). Wavelength calibrations are provided by bracketing Thorium-Argon (Th-Ar) arc lamp exposures.

We used CHIRON to measure the spectroscopic orbit and characterize the host star of KELT-26 b. A total of 15 CHIRON epochs covering all orbital phases of KELT-26 b were obtained. Relative velocities were measured from each spectrum by deriving their stellar line broadening kernels via a Least Squares Deconvolution (LSD) analysis. These velocities are listed in Table 4, and Figure 6 shows the radial velocities as a function of time and phase-folded by the photometric ephemeris.

The absolute radial velocity was estimated by comparing the systemic velocity of KELT-26 in the native CHIRON system to that of four radial velocity standard stars observed by CHIRON in order to determine a mean offset of  $-1.455 \pm 0.037 \text{ km s}^{-1}$  of KELT-26 systemic velocity relative to the CHIRON system. We added the uncertainty in the systemic velocity in the CHIRON system of  $0.025 \text{ km s}^{-1}$  in quadrature to arrive at a final absolute systemic velocity of  $-1.455 \pm 0.045 \text{ km s}^{-1}$ . We corrected the individual CHIRON relative velocities and uncertainties in the same way.



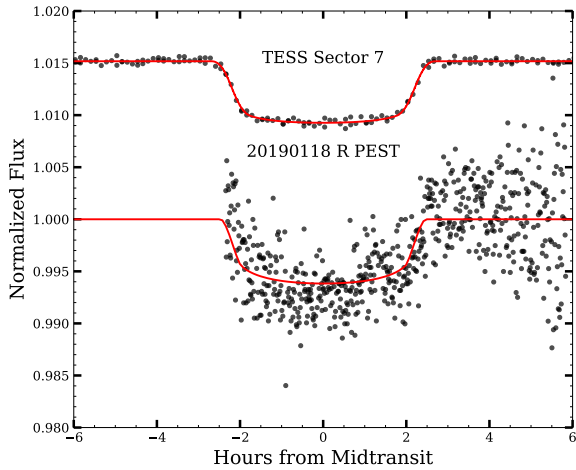


**Figure 4.** The follow-up and *TESS* light curves of KELT-25. The KELT-FUN light curves phase-folded to the ephemeris determined in the global fit (Table 6). Table 2 contains information of all the KELT-FUN observations. The black points are the relative fluxes, while the red line shows the EXOFASTv2 model.

We also used CHIRON to observe the spectroscopic transit of KELT-25b on UT 2019 May 21. A total of 18 spectra were obtained covering the transit, with an integration time of 600 s per exposure. Spectral line profiles were derived from each spectrum as per the procedure described in §3.3. The spectroscopic shadow (i.e., Doppler Tomography signal) of the transiting companion is shown in Figure 7.

### 3.3. Spectroscopic transit of KELT-25 with the Planet Finding Spectrograph

We monitored a transit of KELT-25 b with the Planet Finding Spectrograph (PFS; Crane et al. 2010) on the 6.5 m Magellan-Clay telescope at Las Campanas Observatory, Chile. A total of 19 spectra were obtained on UTC 2019 April 21 spanning 3.3 hours, each observation with an integration time of 600 s. For our observations, PFS was fed by a  $0''.3$  slit, yielding a spectral resolving power of  $R = 130,000$  over the wavelength region of  $3910 - 7340 \text{ \AA}$ . To enable better derivation of the stellar line profiles, the iodine cell was omitted from our observations. Wavelength calibrations were provided by Th-Ar hollow cathode lamp observations obtained at the beginning and end of the night.

Stellar line profiles were derived from each spectrum as per Collier Cameron et al. (2010b) and Donati et al. (1997), via a LSD analysis of the spectra against a non-rotating synthetic template spectrum generated via the ATLAS9 model atmospheres (Castelli & Kurucz 2003). During the transit, the planet sequentially blocks parts of the rotating stellar disk, casting a shadow in our observed rotationally broadened line

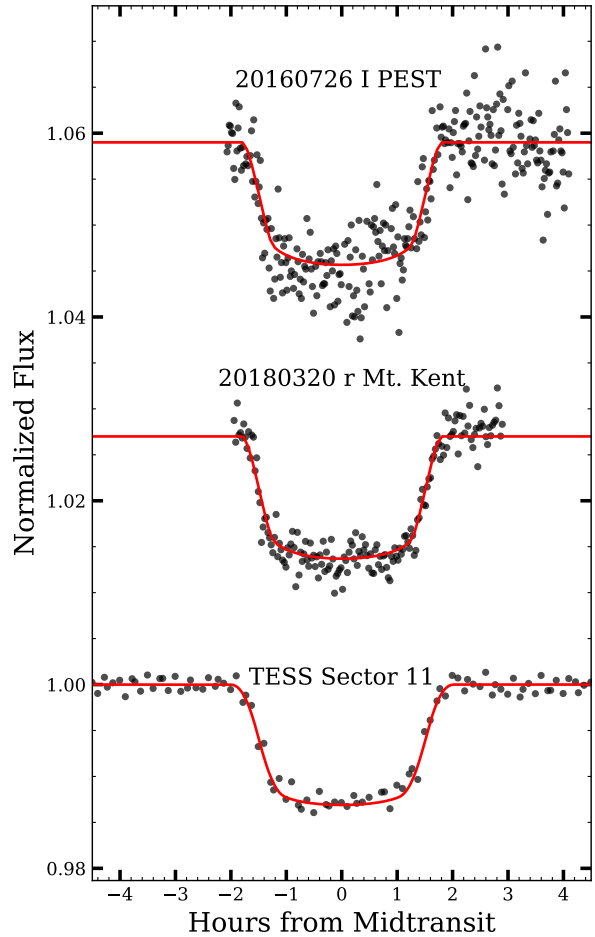


**Figure 5.** The follow-up and *TESS* light curves of KELT-26. The KELT-FUN light curves phase-folded to the ephemeris determined in the global fit (Table 6). Table 2 contains information of all the KELT-FUN observations. The black points are the relative fluxes, while the red line shows the EXOFASTv2 model.

profiles of the star. When we subtract an averaged line profile from each observation, the residuals reveal the spectroscopic transit of the planet as a shadow traversing across the stellar surface. The line profile residuals and best fitting models are shown in Figure 7.

### 3.4. Spectroscopic transit of KELT-26 with MINERVA-Australis

To measure the orbital obliquity and confirm the planetary status of KELT-26 b, we obtained a series of spectroscopic observations during its transit on UT 2019 June 18 via the

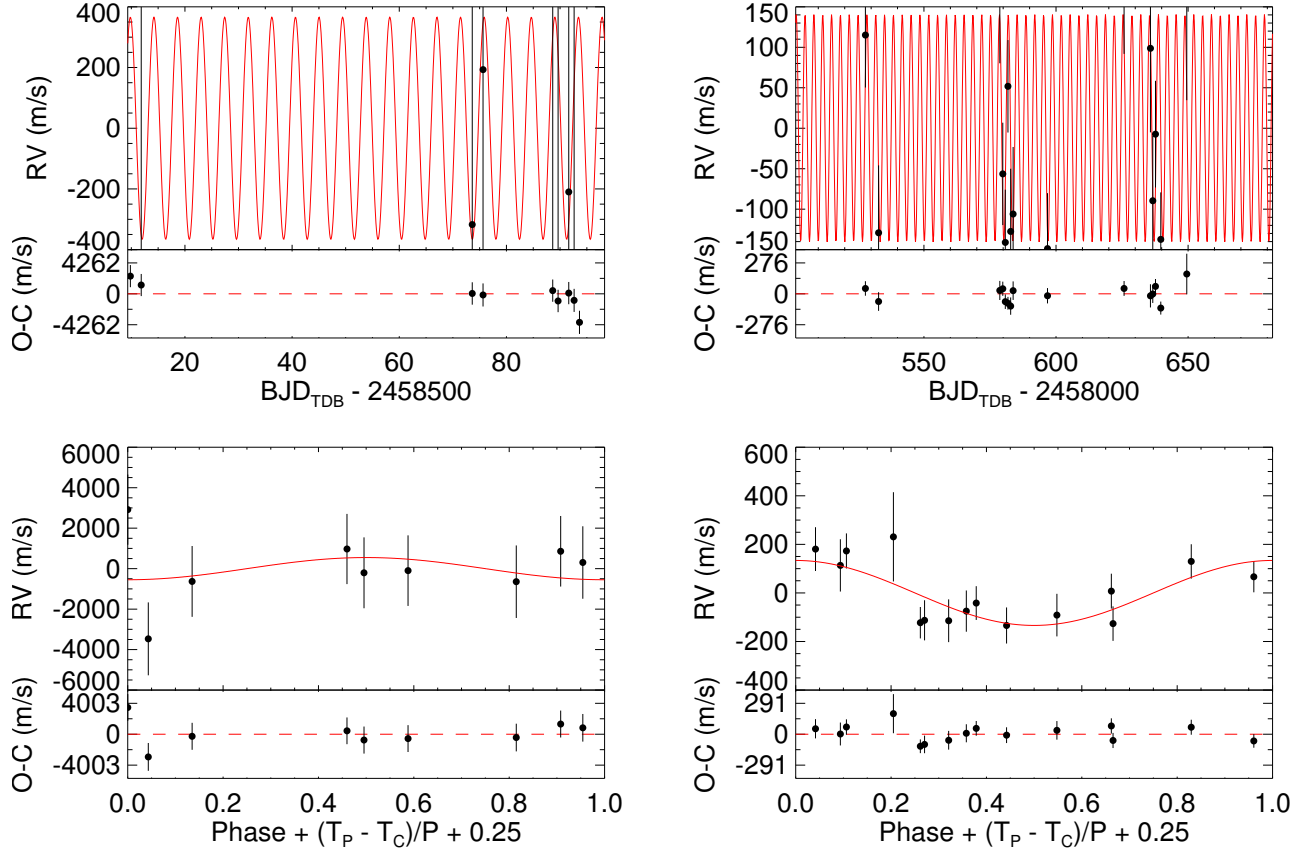


**Figure 6.** (Top) Radial velocity measurements for KELT-25 b from TRES (Left) and KELT-26 b from CHIRON (Right). (Bottom) The radial velocity measurements are phase-folded to the best determined period by EXOFASTv2. The EXOFASTv2 model is shown in red and the residuals to the best-fit are shown below each plot. While we measure the reflex Doppler signal from KELT-26 to  $\sim \sigma_K/K \simeq 30\%$ , and thus are able to constrain the mass of KELT-26 b, we do not obtain a definitive detection of the reflex Doppler signal from KELT-25, and thus are only able to provide an upper limit on the planet mass.

MINIature Exoplanet Radial Velocity Array (MINERVA-Australis) facility, located at the University of Southern Queensland’s Mount Kent Observatory, Australia (Addison et al. 2019). At the time of observations, MINERVA-Australis was operating three active, 0.7m telescopes feeding into a single Kiwispec echelle spectrograph, yielding a resolving power of  $R = 80,000$  over the wavelength region of  $5,000\text{--}6,300\text{ \AA}$ . We made use of data from the two of the three telescopes that yielded the highest signal-to-noise ratio spectra on the night of the transit. Spectral line profiles were derived from each spectrum via the LSD analysis described in Section 3.3. From these observations, we detect the spectroscopic shadow of the transit, finding that the path of the planet is offset from, but parallel to, the projected stellar equator. The spectroscopic transit of KELT-26 b is shown in Figure 7.

#### 4. HIGH-RESOLUTION IMAGING OF KELT-25 b AND KELT-26 b

##### 4.1. Gemini-South Zorro Speckle

We obtained high resolution, speckle images of KELT-25 and KELT-26 to search for nearby companions that could contaminate or dilute the light curves and thus affect the interpretation of the planetary radii, and to rule out sources of false positives like background eclipsing binaries.

Both stars were observed at the Gemini South Observatory using Zorro, a speckle interferometer residing at Gemini-South. Zorro observes in two band-passes simultaneously and is optimized for speckle observations. The observations occurred during instrument commissioning and were the first speckle interferometric science observations made by Zorro. Zorro is a dual-channel imager using two Electron Multiplying CCDs (EMCCDs) as the detectors and containing filter wheels providing bandpass limited observations<sup>5</sup> (see Scott & Howell 2018). The Zorro data was reduced in the standard way as described in Howell et al. (2011) and resulted in spatial reconstructions in each band-pass for KELT-25 and

<sup>5</sup> <https://www.gemini.edu/sciops/instruments/alopeke/>

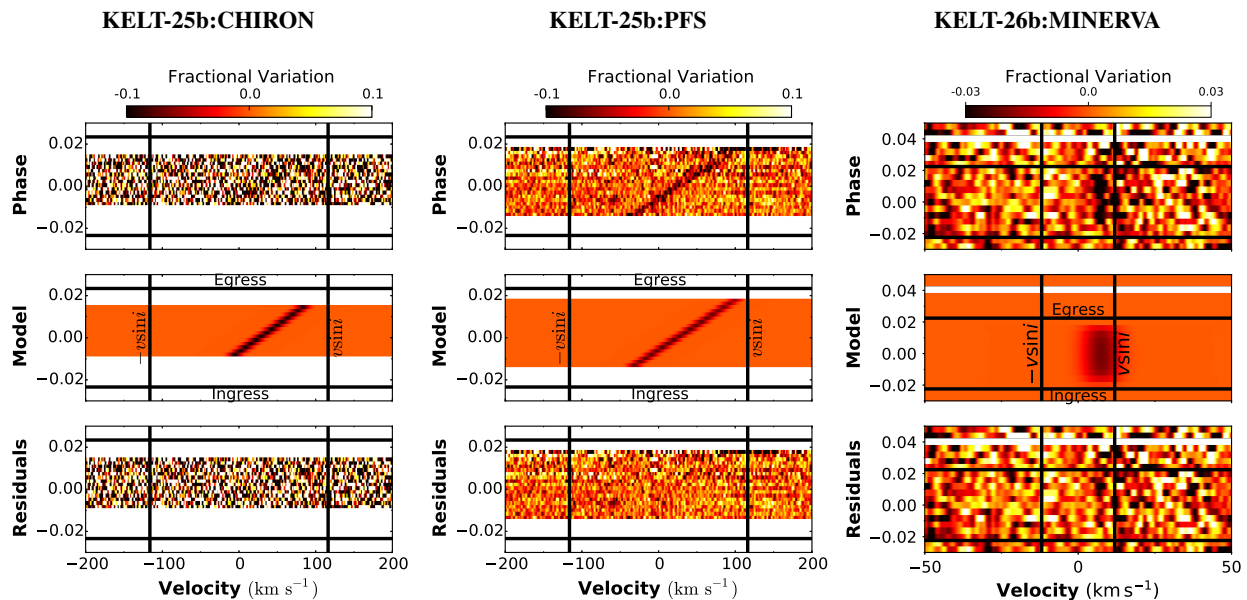


**Figure 7.** The spectroscopic transit signals of KELT-25 from CHIRON (**Left**) and PFS (**Middle**), and KELT-26 from MINERVA-Australis (**Right**). The spectroscopic transit signal shown for KELT-26 from MINERVA-Australis is the combined signal from two telescopes (See §3.4). **Top:** The shadow cast by the planet appears as a dark trail on the line profile residuals. The horizontal axis plots the velocity space of the line profile, while the vertical axis plots the phase, with positive phase increasing upward. The limits of stellar rotation marked by the vertical lines, whereas the beginning and ending of each transit are show with the horizontal lines. **Middle** The best-fit model of the spectroscopic transit is shown. **Bottom:** The residuals after removal of the best fit model, showing a general lack of correlated noise in the line profile subtractions, leading to higher confidence in the detection and a lack of any observable stellar surface oscillations.

KELT-26 providing high contrast, high resolution imaging results.

KELT-25 was observed on UT 2019 May 18 in the blue (562/54 nm) and the red (832/40 nm) bandpasses simultaneously. KELT-25 and KELT-26 observations consisted of 3 sets of 1000 frames with exposure times of 0.06 seconds each, coadded together during the data reduction process. Figure 8 shows the speckle reconstructed image for KELT-25. The 562 nm observations (Figure 8, Top) show no companion star from 17 mas out to  $1''$  within 5 magnitudes of the source, and the 832 nm observations (Figure 8, Bottom) confirm this as well in the red, starting from 28 mas and to a delta magnitude of 6-6.5.

KELT-26 was observed on UT 2019 May 21 in the blue and red bandpasses simultaneously. Figure 9 shows the constraints on possible stellar companions to KELT-26. No stellar companions are detected with angular separation from the primary from 17 mas (562 nm) and 28 mas (832 nm) out to  $1.7''$  and for contrast limits of  $\sim 4.2$  mag (562 nm) and 5-7 mag (832 nm). The black solid line on the contrast curve marks the  $5\sigma$  detection limit.

#### 4.2. Southern Astrophysical Research Speckle (SOAR)

KELT-26 was observed with the speckle camera at the 4.1 m Southern Astrophysical Research (SOAR) telescope on UT 2019 August 12. The instrument and data processing are covered in Tokovinin (2018); a full description of the

SOAR-TESS survey can be found in Ziegler et al. (2019). Figure 10 shows the  $5\sigma$  limit of companion detection, and the inset shows the speckle auto-correlation function (ACF). The speckle ACF is symmetric, but the true quadrant was determined from the shift-and-add image.

A nearby, faint companion was detected at an angular separation of  $2.4096''$  at position angle  $311.15^\circ$  and a magnitude difference of 7.1 mag in  $I_c$  (central wavelength 824 nm, bandwidth 170 nm). This nearby source was not seen in the Gemini-South Zorro observation.

From the contrast magnitude of the neighbor in  $I_c$ , we can estimate its contribution to the flux in the diluted transit light curves. In this case, the contribution of the neighbor is proportional to the ratio of the flux of the secondary to the primary, or 0.14% in  $I_c$ . This estimate agrees with Matson et al. (2018), who found that stellar companions with magnitude contrasts of  $\Delta m \lesssim 7.8$  can only cause  $< 0.1\%$  of a contribution to the flux. This dilution factor reflects the amount by which the true transit depth is diluted and therefore constrains the true radius of the planet. If the true depth is larger by 0.14%, that would represent a  $\sim 1$  sigma difference between the true and reported depths (see Table 6). Therefore, we should, in principle, remove the blended flux from the transit photometry and spectral energy distribution (SED). However, we do not know whether or not the companion is bound to the primary, and we do not have a flux in another band. Thus it

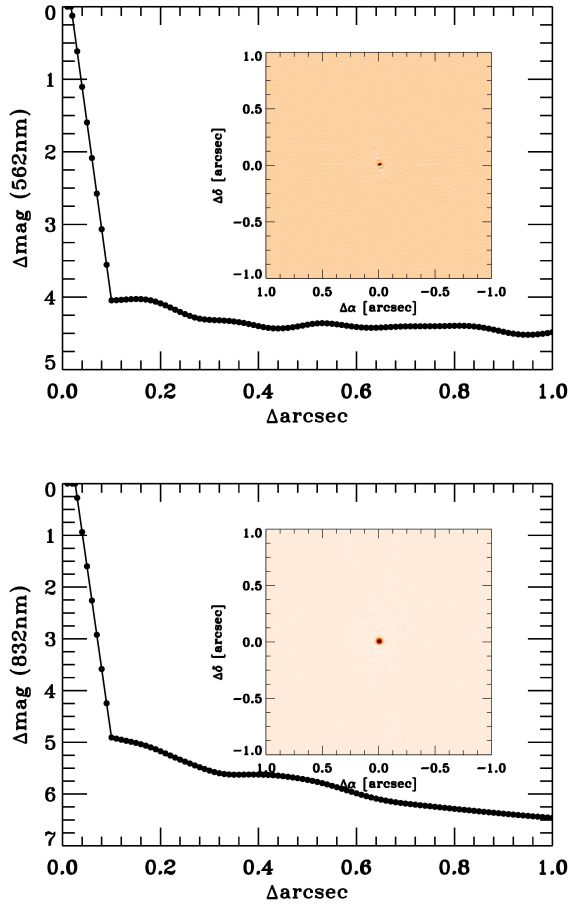


**Figure 8.** Contrast curves and 562 nm image (inset, **Top**) and 832 nm image (inset, **Bottom**) for KELT-25 from Gemini-South with the Zorro instrument (Scott et al. 2019, in prep).

is impossible to estimate the contribution to the flux due to the companion in any band other than  $I_c$ .

The *TESS* bandpass is centered on  $I_c$ , but it is  $\sim 3$  times wider in wavelength space (Ricker et al. 2015), and essentially includes the  $R$ ,  $I_c$  and  $z$  bandpasses. If the primary and the companion had the same SED in the *TESS* bandpass, then the fractional flux contamination would be the same, i.e.,  $\sim 0.14\%$ . This is almost certainly not the case, as the companion is most likely to be either a foreground M star or a background giant. In either scenario, the companion would be fairly red, and thus would produce less fractional flux relative to the primary, which would have a much flatter SED in the *TESS* bandpass. Thus, we take  $0.14\%$  as a conservative upper limit to the blending in the *TESS* bandpass.

Given the blending from the companion, the true depth is larger and therefore the true radius of the planet is larger (Ciardi et al. 2015). The inferred radius of KELT-26 b from the diluted *TESS* and KELT-FUN light curves (all of which were blended by the neighbor in their apertures) is probably larger

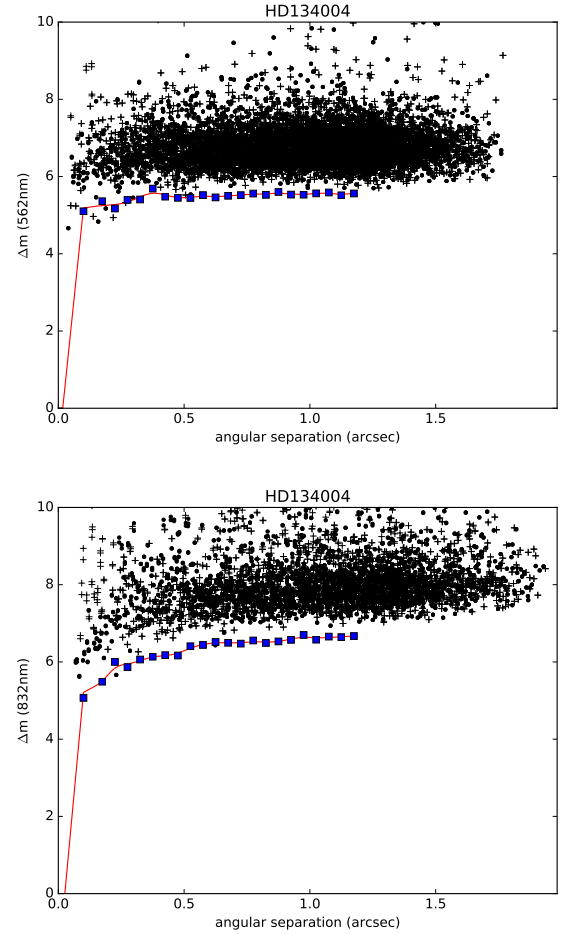


**Figure 9.** Contrast curves and 562 nm image (inset, **Top**) and 832 nm image (inset, **Bottom**) for KELT-26 from Gemini-South with the Zorro instrument (Scott et al. 2019, in prep).

by at most  $\sim 0.5 \times 0.14\%$  or, equivalently,  $0.001R_J$ . This is about  $0.02\sigma$  different from our reported value of the planetary radius, and thus it does not change our qualitative results. This is simply because the uncertainty on the radius of the planet is dominated by the uncertainty on the radius of the star, not the depth of the transit.

Finally, we note that it is possible that this faint companion is an artifact, based on the fact that there are no sources at that position and magnitude found in either *Gaia* DR2 or the *TESS* Input Catalog Version 8 (TIC-8; Stassun et al. 2019). Moreover, if it is a real source, at an angular separation of  $\sim 2.5''$ , it is unlikely to be a bound companion (see, e.g., Matson et al. 2018).

Nevertheless, we encourage more AO/speckle observations in other photometric filters in order to determine if the neighbor is real and bound, and to determine the spectral type of the neighbor and therefore its total flux contribution. This



will enable a more accurate measurements of the transit depth and planetary radius.

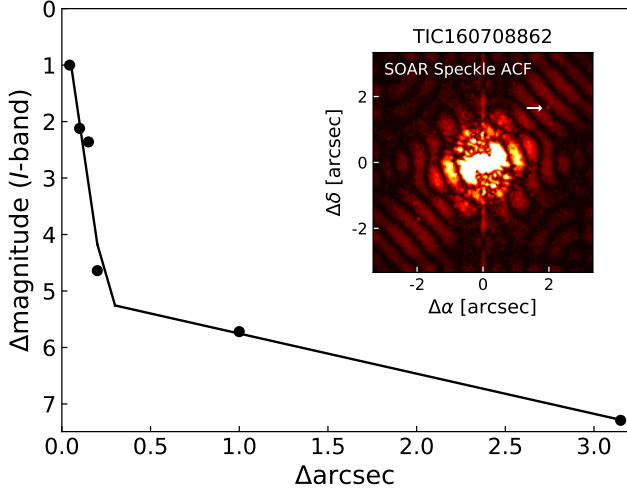


**Figure 10.**  $I_c$  band auto-correlation function of the speckle image for KELT-26 from SOAR. The black points represent the  $5\sigma$  sensitivity limits for KELT-26. The inset shows the auto-correlation function. A white arrow points to the location of the nearby companion. It is located  $2.4096''$  away from the target at  $PA = 311.2^\circ$  and has a magnitude contrast of 7.1 mag in the  $I_c$  band. The companion is mirrored in the ACF on the opposite side due to the speckle processing.

## 5. HOST STAR PROPERTIES

### 5.1. Location and Three-Dimensional Motion in the Galaxy, and Galactic Population

We determine the location in the Galaxy, 3-dimensional (UVW) space motion relative to the local standard of rest, and the inferred population of KELT-25 and KELT-26, using their proper motions, parallaxes, and absolute systemic velocities. Because we have poor metallicity constraints (albeit for different reasons; see the discussion below), we are unable to use this stellar property to help determine the stellar populations of the hosts. However, given that they are both early A stars, we would be surprised if they have significantly subsolar metallicities.

Using the proper motion, *Gaia* parallax (corrected for the [Stassun & Torres 2018b](#) systematic offset of  $-82 \mu\text{as}$ ), and the absolute systemic radial velocity determined as described in §3.1, we compute  $(U, V, W) = (-13.40 \pm 0.58, -13.83 \pm 0.84, -1.24 \pm 0.19) \text{ km s}^{-1}$ , correcting for the velocity of the Sun with respect to the local standard of rest as determined by [Coşkunoglu et al. \(2011\)](#). These velocities imply that the probability of KELT-25 being in the thin disk relative to thick disk is 99.4% using the classification scheme of [Bensby et al. \(2003\)](#). The distance to KELT-25 is  $427.0 \pm 7.8 \text{ pc}$  and it has

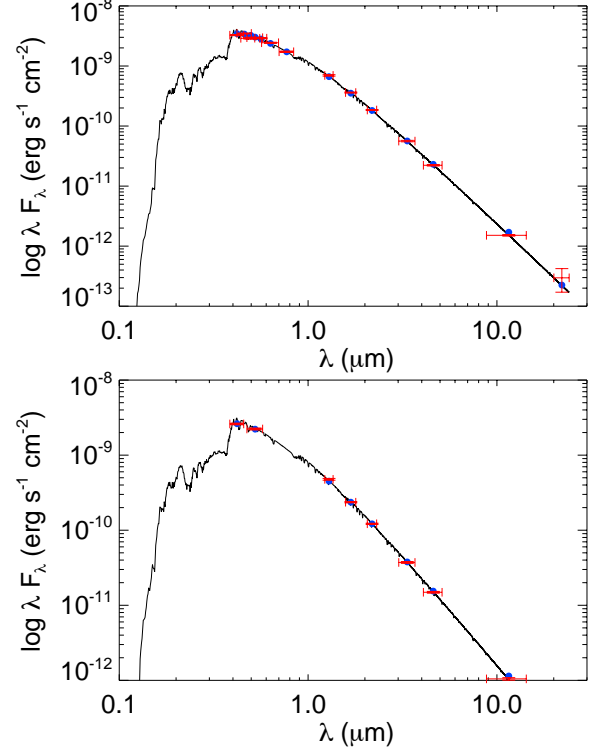


**Figure 11.** The SED fit for KELT-25 (Top) and KELT-26 (Bottom) from our EXOFASTv2 fit. The observed values are shown in red with  $1\sigma$  uncertainties while the predicted integrated fluxes are in blue. The final model is shown by the black line.

Galactic coordinates of  $(\ell, b) = (237.5^\circ, -6.8^\circ)$ . This implies that its vertical ( $Z$ ) distance from the sun is  $Z - Z_\odot = -50.6 \text{ pc}$ . Given that the sun is located at  $Z_\odot \simeq 30 \text{ pc}$  above the plane as determined by the local evolved stellar population according to [Bovy \(2017\)](#), this means that KELT-25 is located only about  $Z \simeq 20 \text{ pc}$  below the plane. This is consistent with the scale height of early A stars as determined by [Bovy \(2017\)](#).

Using the same methodology, we computed  $(U, V, W) = (-24.63 \pm 0.37, 6.75 \pm 0.58, 0.78 \pm 0.20) \text{ km s}^{-1}$  for KELT-26. These velocities imply that the probability of KELT-26 being in the thin disk relative to thick disk is 99.3% using the classification scheme of [Bensby et al. \(2003\)](#). The distance to KELT-26 is  $417.78 \pm 10.5 \text{ pc}$  and it has Galactic coordinates of  $(\ell, b) = (328.19^\circ, +13.32^\circ)$ . This implies that its vertical ( $Z$ ) distance from the sun is  $Z - Z_\odot = 96.1 \text{ pc}$  and  $Z \simeq 126 \text{ pc}$  above the plane. This is roughly twice the typical scale height of an early A star as determined by [Bovy \(2017\)](#), and thus is notable but not completely unexpected.

Both KELT-25 and KELT-26 have roughly the same Galactocentric distance at the sun. Assuming that the distance from the sun to the Galactic center is roughly  $R_0 = 8.2 \simeq \text{kpc}$  ([Gravity Collaboration et al. 2019](#)), we estimate Galactocen-

**Table 5.** Median values and 68% confidence interval for the stellar parameters of KELT-25 and KELT-26 derived from the global fit.

Parameter	Units	Values	
		KELT-25	KELT-26
$M_*$	Mass ( $M_\odot$ )	$2.18^{+0.12}_{-0.11}$	$1.93^{+0.14}_{-0.16}$
$R_*$	Radius ( $R_\odot$ )	$2.264^{+0.048}_{-0.052}$	$1.801^{+0.049}_{-0.048}$
$L_*$	Luminosity ( $L_\odot$ )	$21.8^{+4.6}_{-1.8}$	$16.4^{+3.8}_{-1.8}$
$\rho_*$	Density (cgs)	$0.263^{+0.025}_{-0.018}$	$0.463^{+0.040}_{-0.038}$
$\log g$	Surface gravity (cgs)	$4.064^{+0.032}_{-0.026}$	$4.211^{+0.030}_{-0.033}$
$T_{\text{eff}}$	Effective Temperature (K)	$8280^{+440}_{-180}$	$8640^{+500}_{-240}$
[Fe/H]	Metallicity (dex)	$0.30^{+0.13}_{-0.21}$	$-0.06^{+0.30}_{-0.34}$
[Fe/H] <sub>0</sub>	Initial Metallicity	$0.34^{+0.11}_{-0.19}$	$0.03^{+0.25}_{-0.32}$
Age	Age (Gyr)	$0.46^{+0.14}_{-0.12}$	$0.43^{+0.31}_{-0.25}$
EFP	Equal Evolutionary Phase	$342.0^{+6.3}_{-7.1}$	$331^{+17}_{-28}$
$v \sin I_*$	Projected rotational velocity (km/s)	$114.200 \pm 1.200$	$12.280^{+7.80}_{-8.20}$
$V_{\text{line}}$	Unbroadened line width (m/s)	$3700^{+2300}_{-2400}$	$6400^{+1800}_{-1900}$
$A_V$	V-band extinction (mag)	$0.104^{+0.16}_{-0.073}$	$0.103^{+0.14}_{-0.078}$
$\sigma_{\text{SED}}$	SED photometry error scaling	$2.50^{+0.78}_{-0.53}$	$1.76^{+0.81}_{-0.48}$
$\pi$	Parallax (mas)	$2.366^{+0.041}_{-0.042}$	$2.396 \pm 0.063$
$d$	Distance (pc)	$422.7^{+7.6}_{-7.3}$	$417 \pm 11$

NOTES: †The initial metallicity is the metallicity of the star when it was formed.

‡The Equal Evolutionary Phase corresponds to static points in a star’s evolutionary history when using the MIST isochrones and can be a proxy for age. See §2 in [Dotter \(2016\)](#) for a more detailed description of EEP.

tric distances of 8.4 kpc and 7.8 kpc for KELT-25 and KELT-26, respectively.

## 6. EXOFASTv2 GLOBAL FITS FOR KELT-25 AND KELT-26

To constrain the system parameters, we modeled the available radial velocities, transit photometry, and multiband absolute photometry for KELT-25 and KELT-26 using the exoplanet fitting suite, EXOFASTv2 ([Eastman et al. 2013, 2019; Eastman 2017](#)).

For each system, we globally fit the radial velocities (see §3), the *TESS* and follow-up photometry (see §2.2 and §2.3) and the Doppler tomographic shadows simultaneously (see §3.2, §3.3, and §3.4). Within these fits, we determined the host star properties using a combination of spectroscopic priors, the spectral energy distribution, and the MESA Isochrones and Stellar Tracks (MIST) stellar evolution models ([Dotter 2016; Choi et al. 2016; Paxton et al. 2011, 2013, 2015](#)). For each system, we placed Gaussian priors of [Fe/H] =  $0.0 \pm 0.5$  dex for the metallicity of the host stars, as we did not have reliable constraints from our available spectra. From an independent EXOFASTv2 analysis of the KELT photometry, we adopted a Gaussian prior on the period of KELT-25 b of  $4.401093 \pm 0.000073$  days and on the epoch of  $T_c = 2458493.3144$  BJD<sub>TDB</sub>. Similarly, we placed a Gaussian prior on the orbital period ( $P = 3.344886 \pm 0.000064$  days) and the epoch ( $T_c = 2457482.315 \pm 0.008600$  BJD<sub>TDB</sub>) of KELT-26 b. We also placed priors on the  $v \sin I_*$  from spectroscopy for KELT-25 ( $v \sin I_* = 111.277 \pm 1.422$  km s<sup>-1</sup>)

and KELT-26 ( $v \sin I_* = 9.9349 \pm 1.1333$  km s<sup>-1</sup>) and used parallaxes from *Gaia* DR2 (see Table 1). In addition, we assumed a circular orbit for both systems and we fit for the depth of the secondary eclipse of KELT-25 observed in the lower right panel of Figure 2. We constrained  $A_V$  to the maximum permitted line-of-sight extinction from [Schlegel et al. \(1998\)](#), and the temperature and stellar mass and radius from the SED best-fit values (see Figure 11 for the empirical SEDs of both systems). The best-fitting evolutionary models are shown in Figure 12, and the final fit parameters of the EXOFASTv2 analyses for both stars and their companions are shown in Tables 5 and 6.

Although a global fit to the photometry, radial velocities (including the Doppler Tomography measurements), and the SED can completely constrain the properties of the system, we include constraints from the MIST stellar evolutionary models, which include reasonably well-understood stellar physics, in our global fit. In this manner, we derive best-fit distances to both stars that are slightly different than those inferred from the *Gaia* parallaxes alone. As a result, we find a posterior distribution of the distance of KELT-25 after the global fit of  $422.5^{+7.6}_{-7.3}$  pc, which is  $\sim 0.6$  sigma from that inferred from the *Gaia* parallax (see Table 1). Similarly, for KELT-26, we derive a posterior distance after the global fit of  $417 \pm 11$  pc, which is  $\sim 0.06$  sigma from the distance inferred from the *Gaia* DR2 parallax alone. We consider these differences to be completely consistent within the uncertainties. To calculate the location of KELT-25 and KELT-26 within the Galaxy and their UVW space velocities in §5.1, we opted to use the model-independent parallaxes and distances from *Gaia* DR2. Although in this case these distance measurements are completely consistent, the discovery of larger discrepancy in fits of other systems may have implications for the current stellar evolutionary models or *Gaia* data. Thus the empirical distances from *Gaia* DR2 can serve as a way to test and calibrate the models we use to derive fundamental stellar parameters, or uncover evidence of systematic errors in the *Gaia* data itself.

## 7. DISCUSSION

Both KELT-25 b and KELT-26 b represent extreme transiting systems in a few key aspects. First, KELT-25 b and KELT-26 b both orbit relatively bright ( $V \sim 10$  mag) and extremely hot hosts ( $T_{\text{eff}} \simeq 8300$  K and  $\simeq 8700$  K, respectively), and they also have short orbital periods ( $P \sim 4.4$  and  $P \sim 3.3$  days, respectively). Their proximity to their host stars and their stars’ intrinsic luminosity mean that they receive extreme amounts of stellar radiation, particularly high-energy radiation, resulting in high equilibrium temperatures – assuming zero albedo and complete redistribution – of  $T_{\text{eq}} = 2306$  K (KELT-25 b) and  $T_{\text{eq}} = 2402$  K (KELT-26 b). Both KELT-25 b and KELT-26 b join the recently-defined class of

**Table 6.** Median values and 68% confidence interval for the physical parameters of KELT-25 b and KELT-26 b from the global fit.

Parameter	Description (Units)	Values	Values
		KELT-25	KELT-26
$P$	Period (days)	$4.401131 \pm 0.000059$	$3.3448412 \pm 0.0000033$
$R_p$	Radius ( $R_J$ )	$1.642^{+0.039}_{-0.043}$	$1.940^{+0.060}_{-0.058}$
$M_p$	Mass ( $M_J$ )	(< 64)	$1.41^{+0.43}_{-0.51}$
$T_C$	Time of conjunction (BJD <sub>TDB</sub> )	$2458493.31501 \pm 0.00037$	$2457482.31209^{+0.00090}_{-0.00091}$
$T_0^\dagger$	Optimal conjunction Time (BJD <sub>TDB</sub> )	$2458506.51840 \pm 0.00034$	$2458321.86724^{+0.00038}_{-0.00039}$
$a$	Semi-major axis (AU)	$0.0681^{+0.0012}_{-0.0011}$	$0.0545^{+0.0013}_{-0.0015}$
$i$	Inclination (Degrees)	$85.37^{+0.55}_{-0.42}$	$84.45^{+0.39}_{-0.41}$
$T_{eq}$	Equilibrium temperature (K)	$2306^{+100}_{-47}$	$2402^{+130}_{-71}$
$\tau_{circ}$	Tidal circularization timescale (Gyr)	$-0.1^{+4.1}_{-3.9}$	$0.053^{+0.019}_{-0.020}$
$K$	RV semi-amplitude (m/s)	(< 4687.8)	$123^{+37}_{-45}$
$\log K$	Log of RV semi-amplitude	(< 3.64)	$2.09^{+0.11}_{-0.20}$
$R_p/R_*$	Radius of planet in stellar radii	$0.07450^{+0.00039}_{-0.00042}$	$0.11066^{+0.00090}_{-0.00087}$
$a/R_*$	Semi-major axis in stellar radii	$6.46^{+0.20}_{-0.15}$	$6.49 \pm 0.18$
$\delta$	Transit depth (fraction)	$0.005550^{+0.000059}_{-0.000062}$	$0.01225^{+0.00020}_{-0.00019}$
$\tau$	Ingress/egress transit duration (days)	$0.0192^{+0.0011}_{-0.0012}$	$0.0238^{+0.0016}_{-0.0014}$
$T_{14}$	Total transit duration (days)	$0.2051^{+0.0013}_{-0.0015}$	$0.1514 \pm 0.0016$
$T_{FWHM}$	FWHM transit duration (days)	$0.18586^{+0.00097}_{-0.00096}$	$0.12760^{+0.00098}_{-0.00099}$
$b$	Transit Impact parameter	$0.522^{+0.034}_{-0.048}$	$0.628^{+0.027}_{-0.029}$
$\delta_{S,3.6\mu m}$	Blackbody eclipse depth at $3.6\mu m$ (ppm)	$732^{+27}_{-23}$	$1664^{+82}_{-72}$
$\delta_{S,4.5\mu m}$	Blackbody eclipse depth at $4.5\mu m$ (ppm)	$872^{+26}_{-24}$	$1965^{+83}_{-74}$
$\rho_p$	Density (cgs)	(< 18.3)	$0.238^{+0.077}_{-0.088}$
$\log g_p$	Surface gravity	(< 4.77)	$2.97^{+0.12}_{-0.20}$
$\lambda$	Projected Spin-orbit alignment (Degrees)	$23.4^{+3.2}_{-2.3}$	$91.3^{+6.5}_{-6.3}$
$\Theta$	Safronov Number	$-0.01^{+0.50}_{-0.48}$	$0.041^{+0.012}_{-0.015}$
$\langle F \rangle$	Incident Flux ( $10^9 \text{ erg s}^{-1} \text{ cm}^{-2}$ )	$6.42^{+1.2}_{-0.51}$	$7.56^{+1.7}_{-0.86}$
$T_p$	Time of Periastron (BJD <sub>TDB</sub> )	$2458493.31501 \pm 0.00037$	$2457482.31209^{+0.00090}_{-0.00091}$
$T_S$	Time of eclipse (BJD <sub>TDB</sub> )	$2458495.51558 \pm 0.00036$	$2457483.98451 \pm 0.00090$
$T_A$	Time of Ascending Node (BJD <sub>TDB</sub> )	$2458496.61586 \pm 0.00035$	$2457484.82072 \pm 0.00090$
$T_D$	Time of Descending Node (BJD <sub>TDB</sub> )	$2458494.41530 \pm 0.00036$	$2457483.14830 \pm 0.00090$
$M_p \sin i$	Minimum mass ( $M_J$ )	(< 64)	$1.40^{+0.43}_{-0.51}$
$M_p/M_*$	Mass ratio	(< 0.028)	$0.00070^{+0.00021}_{-0.00026}$
$d/R_*$	Separation at mid transit	$6.46^{+0.20}_{-0.15}$	$6.49 \pm 0.18$
$P_T$	A priori non-grazing transit prob	$0.1433^{+0.0035}_{-0.0043}$	$0.1370^{+0.0039}_{-0.0036}$
$P_{T,G}$	A priori transit prob	$0.1664^{+0.0041}_{-0.0051}$	$0.1710^{+0.0050}_{-0.0047}$
Telescope Parameters:		TRES	CHIRON
$\gamma_{rel}$	Relative RV Offset (m/s)	$720^{+810}_{-820}$	$-25595^{+25}_{-24}$
$\sigma_J$	RV Jitter (m/s)	$2240^{+1100}_{-620}$	$67^{+32}_{-23}$

**NOTES:**  $\dagger$  Minimum covariance with period. All values in this table for the secondary occultation of KELT-25 b are predicted values from our global analysis. All values in red are  $3\sigma$  upper limits on mass dependent parameters for KELT-25 b.

planets of ‘‘Ultra Hot Jupiters’’, which, similar to the prototype WASP-33b (Collier Cameron et al. 2010a), are primarily planets on short-period orbits around early A stars. They are thus among the hottest transiting exoplanets known. Indeed, the equilibrium temperatures (zero albedo, complete heat distribution) of these planets are commonly in excess of 2000 K, and it seems likely that their day-side temperatures would be markedly higher still (see Figure 13), and likely have day-side temperatures that are much higher.

Our EXOFASTv2 models (Table 6) indicate that the radii of both planets are also significantly inflated ( $R_p = 1.64R_J$  and  $R_p = 1.94R_J$ ). From an irradiation evolution analysis of these systems (see §7.3), we conclude that these objects currently receive an insolation flux of around  $5 \times 10^9 \text{ erg s}^{-1} \text{ cm}^{-2}$  (KELT-25 b) and  $1 \times 10^{10} \text{ erg s}^{-1} \text{ cm}^{-2}$  (KELT-26 b).

Moreover, their orbital histories suggest that they probably have always been above the Demory & Seager (2011) insolation threshold of  $2 \times 10^8 \text{ erg s}^{-1} \text{ cm}^{-2}$ , which is an empirical threshold above which giant planets exhibit significant radius inflation. For this reason, it is not surprising that they are both highly inflated. The extreme temperatures of these companions and the optical and infrared brightness of their hosts (KELT-25:  $V = 9.65$ ,  $J = 9.36$ ; KELT-26:  $V = 9.96$ ,  $J = 9.77$ ) mean that the prospects for detailed atmospheric characterization via transmission spectroscopy with James Webb Space Telescope (JWST) or the Hubble Space Telescope (HST) are promising. Indeed, the TESS light curve for KELT-25 (Figure 2) demonstrates the weak but significant detection of the secondary eclipse of the system, as the planet moves behind the star. Given the estimated equilib-

**Table 7.** Median values and 68% confidence interval for global model of KELT-25 and KELT-26 from the global fit.

KELT-25 b			
Wavelength Parameters:		R	TESS
$u_1$ . . . . .	linear limb-darkening coeff . . . . .	$0.292 \pm 0.049$	$0.159 \pm 0.029$
$u_2$ . . . . .	quadratic limb-darkening coeff . . . . .	$0.348 \pm 0.049$	$0.260 \pm 0.035$
$A_T$ . . . . .	Secondary eclipse depth (ppm) . . . . .	–	$187 \pm 46$
Transit Parameters:		PEST UT 2019-01-18 (R)	TESS Sector 7 TESS Sector 7 (secondary)
$\sigma^2$ . . . . .	Added Variance . . . . .	$0.00000779^{+0.00000062}_{-0.00000058}$	$-0.0000000863^{+0.0000000057}_{-0.0000000050}$
$F_0$ . . . . .	Baseline flux . . . . .	$1.00362 \pm 0.00013$	$0.999826 \pm 0.000049$ $0.999811 \pm 0.000040$
Doppler Tomography Parameters:			
$\sigma_{DT}$ . . . . .	Doppler Tomography Error scaling	$0.9975^{+0.0100}_{-0.0098}$	$0.9839^{+0.0057}_{-0.0056}$
KELT-26 b			
Wavelength Parameters:		I	r' TESS
$u_1$ . . . . .	linear limb-darkening coeff . . . . .	$0.185 \pm 0.048$	$0.207 \pm 0.045$ $0.212 \pm 0.044$
$u_2$ . . . . .	quadratic limb-darkening coeff . . . . .	$0.264 \pm 0.051$	$0.279 \pm 0.048$ $0.280 \pm 0.047$
Transit Parameters:		PEST UT 2016-07-26 (I)	CDK700 UT 2018-03-20 (r') TESS UT 2019-04-07 (TESS)
$\sigma^2$ . . . . .	Added Variance . . . . .	$0.00000780^{+0.00000010}_{-0.00000089}$	$0.00000170^{+0.000000025}_{-0.00000021}$ $0.000000420^{+0.000000029}_{-0.000000027}$
$F_0$ . . . . .	Baseline flux . . . . .	$0.99573 \pm 0.00021$	$0.99891 \pm 0.00015$ $1.000000 \pm 0.000026$
Doppler Tomography Parameters:			
$\sigma_{DT}$ . . . . .	Doppler Tomography Error scaling	MINERVA 3 $0.991 \pm 0.013$	MINERVA 4 $0.997 \pm 0.012$

rium temperature of the star, this flux decrement is also certainly caused by the tail of the thermal emission from the planet. We estimate a secondary eclipse depth of  $\sim 187 \pm 46$  ppm (see Table 7), implying a brightness temperature of the planet in the *TESS* band of  $\sim 3396^{+140}_{-170}$  K, which is substantially higher than the equilibrium temperature (assuming zero albedo and complete heat redistribution) of  $2303^{+100}_{-47}$  K.

To better place these planets in context of all systems with measured rotation rates and projected spin-orbit misalignments, we highlight KELT-25 and KELT-26 in Figures 17 and 18 showing the distributions of  $v \sin I_*$  and spin-orbit misalignments  $\lambda$  versus stellar temperature for A stars ( $v \sin I_*$  distribution) and all known planet hosts with measured spin-orbit angles. Figure 13 shows a plot of atmospheric scale height as a function of equilibrium temperature for all the known transiting exoplanets with measured masses. KELT-26 b has a large scale height and receives extreme amounts of UV radiation from its host. With KELT-25 b and KELT-26 b, we have a large enough sample of A-stars with transiting exoplanets that we can begin to see emerging patterns in the population (see Table 8). Perhaps one such interesting trend is the gap in planet equilibrium temperatures between roughly 2600 K and 4000 K, visible in Figure 13. We still do not understand whether this gap is real or the result of selection effects. All the confirmed planets around A stars have short periods ( $1.22 < P < 4.79$  days) and transit bright host stars ( $V \lesssim 10$ ), which, as previously remarked, make them attractive targets for atmospheric characterization with the upcoming *JWST*. Before *JWST* launches, however, *TESS* may be able to observe these planets in tran-

sit, in some cases even resolving their secondary eclipses, as with KELT-25 b. These observations can constrain the brightness temperature of these planets and therefore provide insights into the heat distribution mechanisms of their atmospheres.

### 7.1. *KELT-26 b: A giant planet orbiting a likely Am star with a likely significant transit asymmetry*

KELT-26 b orbits a relatively young ( $\sim 430$  Myr), slowly rotating A star ( $v \sin I_* = 12.2$  km s $^{-1}$ ). This rotational velocity is rather atypical for an early A star, as such stars tend to be much faster rotators on average. From the Doppler tomographic observations (see §3), we also measured the projected spin-orbit angle of this system, and conclude that it is on an orbit that is consistent with being exactly parallel to the projected stellar equator, with  $\lambda = 91.3^{+6.5}_{-6.3}$ . However, the orbit is likely not polar, because the impact parameter of planet’s transit is  $b \simeq 0.6$  and therefore the planet is not transiting exactly across the pole of the star. The projected spin-orbit alignment  $\lambda$  need not be the true true obliquity  $\psi$ , which is a more fundamental quantity of the system. However, the latter is harder to constrain, as explained in Johnson et al. (2018), because it requires knowledge of both the planetary orbital inclination  $i$  as well as the stellar spin axis  $I_*$ . The observation of an orbit that has  $\lambda \sim 90^\circ$  with the unusually slow rotation period of KELT-26 ( $v \sin I_* = 12.2$  km s $^{-1}$ ) may imply that the star is perhaps spinning faster but we are observing it nearly pole-on. The phase-folded *TESS* light curve of the primary (Figure 3) appears to show a slight asymmetry, such that the planet is first passing over a region of the star with higher-than average surface brightness, whereas the



**Table 8.** A-star transiting planet hosts from the literature ordered by decreasing stellar temperature

Planet	$M_p$ ( $M_J$ )	$R_p$ ( $R_J$ )	$T_{\text{eff}}$ (K)	$P$ (days)	$L_*$ ( $L_\odot$ )	$T_{\text{eq}}$ (K)	$\lambda$ (deg)	SpT	Ref.
KELT-9b	$2.88 \pm 0.84$	$1.891^{+0.061}_{-0.053}$	$10170 \pm 450$	1.48	$53^{+13}_{-10}$	$4050 \pm 180$	$-84.8 \pm 1.4$	A0	1
KELT-20b/MASCARA-2b	$< 3.5$ ( $3\sigma$ )	$1.735^{+0.07}_{-0.075}$	$8730^{+250}_{-260}$	3.47	$12.7^{+2.2}_{-1.9}$	$\sim 2250$	$3.4 \pm 2.1$	A2	2
KELT-26 b	$1.41^{+0.43}_{-0.51}$	$1.940^{+0.060}_{-0.058}$	$8640^{+500}_{-240}$	3.34	$16.4^{+3.8}_{-1.8}$	$2402^{+130}_{-71}$	$91.3^{+6.5}_{-6.3}$	A3m	3
HAT-P-70b	$< 6.14$	$2.011^{+0.051}_{-0.114}$	$8450^{+540}_{-690}$	2.74	$16.7^{+5.3}_{-4.6}$	$2562^{+43}_{-52}$	$116.5^{+3.5}_{-3.8}$	A3V	4
KELT-25 b	$< 64$	$1.642^{+0.039}_{-0.043}$	$8280^{+440}_{-180}$	4.40	$21.8^{+4.6}_{-1.8}$	$2306^{+100}_{-47}$	$23.4^{+3.2}_{-2.3}$	A4	5
WASP-189b	$2.13 \pm 0.28$	$1.374 \pm 0.082$	$8000 \pm 100$	2.72	$1.293 \pm 0.045$	$2641 \pm 34$	$89.3 \pm 1.4$	A6IV-V	6
HATS-70b	$12.9^{+1.8}_{-1.6}$	$1.384^{+0.079}_{-0.074}$	$7930^{+630}_{-820}$	1.89	$12.0^{+5.5}_{-3.4}$	$2730^{+140}_{-160}$	$8.9^{+5.6}_{-4.5}$	A6V	7
MASCARA-4b	$3.1 \pm 0.9$	$1.53^{+0.07}_{-0.04}$	$7800 \pm 200$	2.82	$12.23 \pm 0.655$	$2100 \pm 100$	$247.5^{+1.5}_{-1.7}$	A7V	8
Kepler-13Ab	$\sim 9.2 \pm 1.1$	$1.512 \pm 0.035$	$7650 \pm 250$	1.76	-	$2550 \pm 80$	$58.6 \pm 2.0$	A8V	9
KELT-21b	$< 3.91$ ( $3\sigma$ )	$1.586^{+0.039}_{-0.040}$	$7598^{+81}_{-84}$	3.61	$8.03^{+0.54}_{-0.53}$	$2051^{+29}_{-30}$	$-5.6^{+1.7}_{-1.9}$	A8V	10
MASCARA-1b	$3.7 \pm 0.9$	$1.5 \pm 0.3$	$7554 \pm 150$	2.14	$13.1 \pm 3$	$2570^{+50}_{-30}$	$69.5 \pm 3$	A8V	11
HAT-P-57b	$1.41 \pm 1.52$	$1.74 \pm 0.36$	$7500 \pm 250$	2.46	$6.4 \pm 1.1$	2200	$-16.7$ -3.3 or $2.76$ -57.4	A8V	12
KELT-19Ab	$1.62^{+1.8}_{-0.20}$	$1.83 \pm 0.10$	$7500 \pm 110$	4.61	$9.5^{+1.2}_{-1.1}$	$\sim 1935$	$-179.7^{+3.7}_{-3.8}$	Am	13
KELT-17b	$1.31^{+0.28}_{-0.29}$	$1.525^{+0.065}_{-0.060}$	$7454 \pm 49$	3.08	$7.51^{+0.62}_{-0.55}$	$2087^{+32}_{-33}$	$-115.9 \pm 4.1$	A9V	14
WASP-33b	4.1	$1.497 \pm 0.045$	$7430 \pm 100$	1.22	-	$2710 \pm 50$	$251.6 \pm 0.7$	A9V	15
HAT-P-69b	$3.54^{+0.61}_{-0.60}$	$1.714 \pm 0.028$	$7394^{+360}_{-600}$	4.79	$10.0^{+1.8}_{-0.9}$	$1930^{+80}_{-230}$	$16.5^{+2.1}_{-1.9}$	A9V	16

**NOTES:**

References: 1. Gaudi et al. (2017) 2. Lund et al. (2017); Talens et al. (2018) 3. This work 4. Zhou et al. (2019b) 5. This work 6. Anderson et al. (2018) 7. Zhou et al. (2019b) 8. Dorval et al. (2019) 9. Shporer et al. (2011); Esteves et al. (2015); Johnson et al. (2014) 10. Johnson et al. (2018) 11. Talens et al. (2017) 12. Hartman et al. (2015) 13. Siverd et al. (2018) 14. Zhou et al. (2016) 15. Collier Cameron et al. (2010b) 16. Zhou et al. (2019a)

planet later passes over a region of the star with lower surface brightness. This would be expected from gravity darkening, assuming the planet first passes over or near the pole, and then over the lower surface brightness equator (Barnes 2009). Gravity darkening has already been observed with *TESS* for two hot Jupiters: HAT-P-69b (TOI 625.01) and HAT-P-70b (TOI 624.01) (Zhou et al. 2019b), and is also clear in the unpublished *TESS* light curve of KELT-9 (Wong et al. (2019), Wachiraphan et al.; Ahlers et al., in preparation). However, as we discuss below, the host star KELT-26 also appears to be variable at the  $\sim$ few millimagnitude level at a period that is nearly commensurate (1:18) with the period of the planet. This variability may also be causing the slight asymmetry.

A Lomb-Scargle periodogram (Lomb 1976; Scargle 1982) of the light curve of KELT-26 shows a significant peak at a period of 0.185 days, with an amplitude of 0.115%, or 1.25 mmag. This period is nearly 1/18 (1/18.06, to be precise) of the period of the planet. We do not know if this is simply a coincidence, as the mass of the companion is likely too small to induce periodic oscillations on its host star. Both KELT-25 and KELT-26 are inside the instability strip, where one might expect to find  $\delta$  Scuti pulsations. Indeed, the period and amplitude of the variability of KELT-26 are consistent with other  $\delta$  Scuti variables. A more detailed study of the nature of the intrinsic variability of KELT-26 is beyond the scope of this paper.

On the other hand, the spectrum of KELT-26 shows evidence of being an Am star (or "metallic-line A star"). Am stars typically rotate much more slowly than A stars of the

same effective temperature. This is usually attributed to a stellar companion that has spun down the star or otherwise "stolen" its angular momentum at birth. However, we find no evidence of a stellar companion which would affect the spin rate of KELT-26, and the planetary companion is not sufficiently massive to play this role. Am stars are typically identified by the fact that the star does not appear to have a consistent metallicity when measured using absorption lines formed at different depths in the photosphere. This can be seen in Figure 14, where it is clear that for models with a fixed  $T_{\text{eff}}$  and varying [Fe/H], no single model can simultaneously fit all of the spectral lines.

### 7.2. KELT-25 b: A substellar object transiting a rapidly rotating, young A star and likely cluster member

With a  $v \sin I_*$  of  $114.2 \text{ km s}^{-1}$ , KELT-25 is rotating much faster than KELT-26, and this has implications for the dynamical history of its potential planet. In this case, the classical scenario of hot Jupiters spiraling towards their host stars is reversed. The stellar tidal dissipation causes the semi-major axis of KELT-25 b's orbit to gradually increase (see §7.3). As a result, KELT-26 b will avoid getting engulfed by its host star, at least until the star leaves the main sequence. The Doppler tomography shadows (Figure 7) suggest that it is on a prograde, aligned orbit ( $\lambda = 23.4^{+3.2}_{-2.3}$ ). To estimate the age of the systems, we show a modified Hertzsprung-Russell diagram ( $\log g_*$  vs  $T_{\text{eff}}$ ) in Figure 12. From the MIST stellar evolutionary models, and taking the 1-sigma upper limit on the mass for KELT-25, we infer an age of  $0.46^{+0.14}_{-0.12}$  Gyr. Using

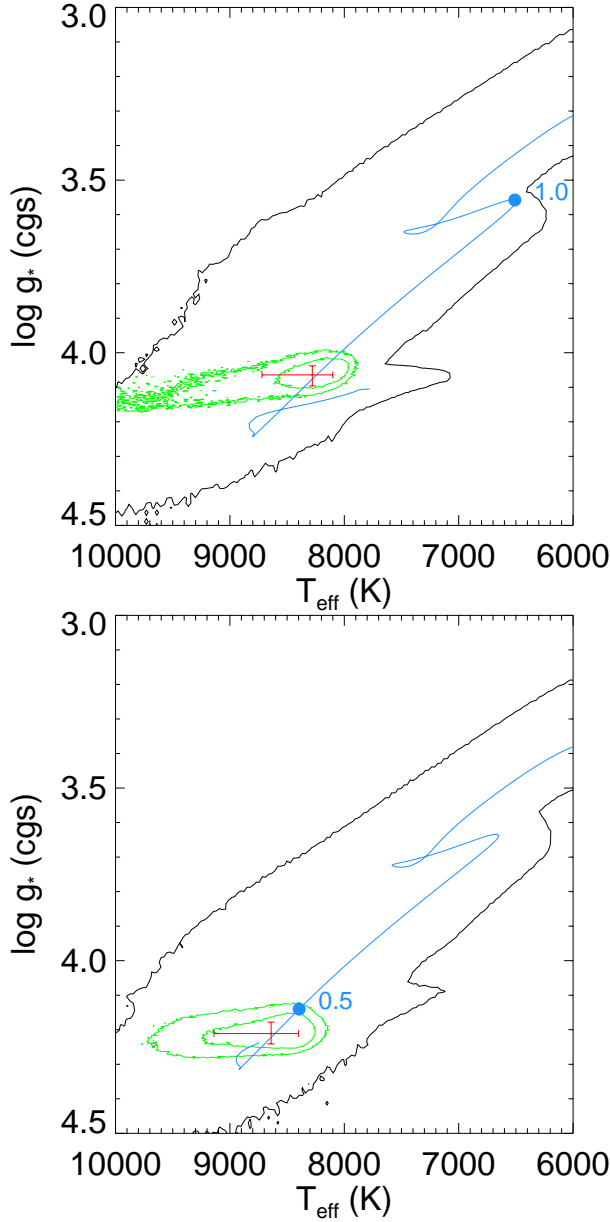


**Figure 12.** The best-fitting MIST track for KELT-25 (**Top**) and KELT-26 (**Bottom**) shown by the blue line. The black line shows the  $3\sigma$  contours for the MIST evolutionary tracks. The red data point shows the median values and  $1\sigma$  uncertainties from our global fit, while the green contours correspond to the  $3\sigma$  errors. The blue points mark the location of 1.0 (**Top**) and 0.5 Gyr (**Bottom**) along the MIST track.

the same models, we obtain an age for KELT-26 of  $0.43^{+0.31}_{-0.25}$  Gyr.

### 7.2.1. Is KELT-25 a member of a stellar cluster, association, or moving group?

We cross-matched existing *TESS* Objects of Interest (TOIs) to the catalog of clusters presented in Kounkel &

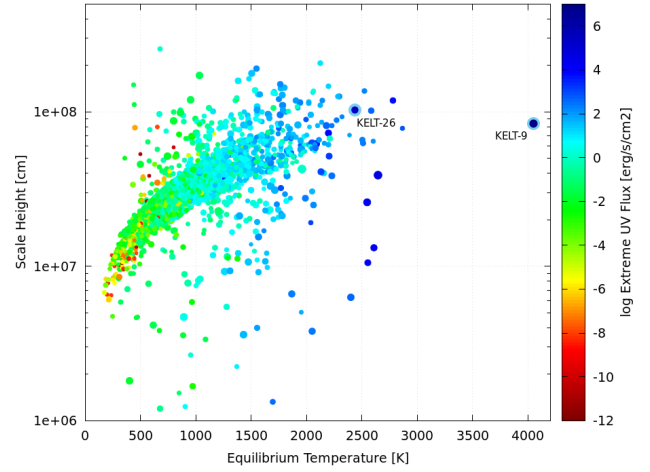


**Figure 13.** This scatter-plot shows the atmospheric scale height versus equilibrium temperature for all the known transiting exoplanets with mass measurements. The color scale corresponds to the extreme ultraviolet radiation that planets receive from their host stars. The symbol sizes are inversely proportional to the magnitude in V-band of the host stars. At  $T_{\text{eq}} \sim 2402$  K, KELT-26 b stands out as one of the hottest known exoplanets, receiving extreme amounts of UV radiation, likely resulting in the exceptionally large radius of  $R_p \sim 1.9R_J$ , and subsequent large scale height.

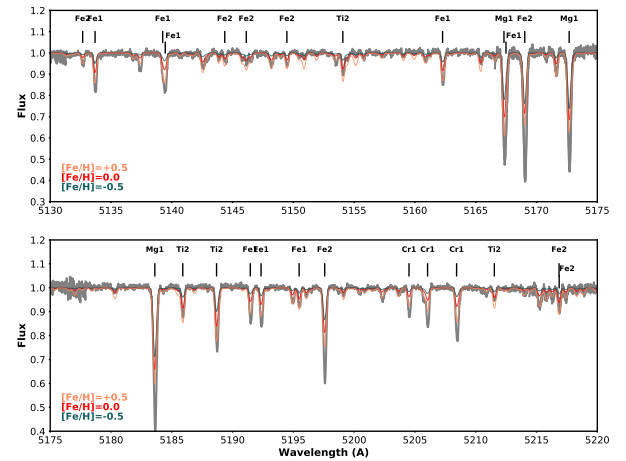


**Figure 14.** A portion of the CHIRON spectrum near the Mgb region for KELT-26 is shown in grey. The other lines show a set of  $T_{\text{eff}} = 9000$  K,  $\log g_* = 4.25$  synthetic spectra with  $[\text{Fe}/\text{H}]$  of  $-0.5$  (green),  $0.0$  (red), and  $+0.5$  dex, generated with the ATLAS9 model atmospheres (Castelli & Kurucz 2003), demonstrating that a single  $[\text{Fe}/\text{H}]$  cannot simultaneously fit all of observed spectral features.

Covey (2019), and we found a match between TOI-626.01 (KELT-25) and one of the putative clusters identified in that paper as Theia 449. In that paper, they identified 1900 clusters from an analysis of the distribution of sources in

5-dimensional space (three-dimensional position and two-dimensional (e.g., transverse) velocity) in *Gaia* DR2. They then performed a clustering analysis on *Gaia* sources within  $|b| < 30^\circ$  of the Galactic plane and parallaxes with  $\pi > 1$  mas using a Python implementation of HDBSCAN (Hierarchical Density-Based Spatial Clustering of Applications with Noise, McInnes et al 2017). They estimated ages of their clusters and associations applying a combination of machine learning and isochronal fitting techniques to determine the ages of their sources to a precision of  $\sim 0.15$  dex.

For the cluster Theia 449, Kounkel & Covey (2019) report a mean Galactic latitude of  $b = -7.13^\circ$ , a mean parallax of  $2.37 \pm 0.82$  mas, an age of 0.162 Gyr and mean radial velocity of  $23.54 \pm 18.21$  km s $^{-1}$ . From our MIST models, we determine KELT-25 is a young A star, with an age of  $0.46^{+0.14}_{-0.12}$  Gyr, which is just  $\sim 2$ -sigma discrepant with the mean reported age of the cluster. Our derived properties for KELT-25 are thus in general agreement with the average properties of Theia 449. However, the broader issue of whether Theia 449 truly represents a collection of coeval stars is outside the scope of this paper. Clarification of the status of Theia 449 could help resolve the age, metallicity, and formation environment of KELT-25.

### 7.2.2. Is KELT-25 b a planet or brown dwarf?

Given its extremely fast rotation, we were only able to constrain the mass of KELT-25 b to a  $3\sigma$  upper limit of  $\sim 64 M_J$ , or a  $1\sigma$  upper limit of  $5.46 M_J$ . We argue that KELT-25 b is likely to be a planet or low-mass brown dwarf based on several lines of reasoning. First, substellar companions at the upper end of the allowed mass range and with this period are known to be relatively rare (the so-called "brown dwarf desert" (e.g., Grether & Lineweaver 2006). Second, no brown dwarfs (BDs) are known that are as highly inflated as KELT-25 b (Zhou et al. 2019a). Inspection of Figure 9 of Zhou et al. (2019a) reveals that not only do no BD have radii as large as KELT-25 b, only about a dozen lower-mass transiting planets have radii this large. Given the large surface gravity expected if KELT-25 b had a mass significantly above the deuterium burning limit, this is strong circumstantial evidence that it is less massive. Finally, there is no evidence of Doppler beaming (Loeb & Gaudi 2003) or ellipsoidal variability (Drake 2003) in the KELT-25 b *TESS* light curve, which would likely be expected if KELT-25 b had a mass substantially above the deuterium burning limit. The weight of evidence indicates that KELT-25 b is most likely a giant planet or very low-mass brown dwarf.

### 7.2.3. Intrinsic Variability of KELT-25

As mentioned previously, both KELT-25 and KELT-26 are inside the instability strip. Only about 40% of stars within this range of  $T_{\text{eff}}$  show  $\delta$  Scuti pulsations (Murphy et al. 2019;

see their Fig. 11). While KELT-26 does show variability consistent with  $\delta$  Scuti pulsations (see §7.1), we find no evidence of intrinsic variability in the KELT-25 *TESS* light curve.

### 7.3. Tidal Evolution and Irradiation History

We estimated the orbital and irradiation evolution of KELT-25 and KELT-26; in particular, we calculated the history of the companions' semi-major axis and irradiation as a function of stellar age using the Planetary Orbital Evolution due to Tides (POET; Penev et al. 2014). POET assumes a constant tidal phase lag or quality factor  $Q_*$ , a circular orbit, and no perturbations in the orbits due to unseen stellar or planetary companions. We further assumed that the tides raised by the planet or substellar companion are negligible and that the evolution of the planet's orbit is therefore dominated by the dissipation of tidal perturbations in the star (as explained in Rodriguez et al. 2019b). We accounted for the changes in stellar radius and luminosity in time by using a MIST stellar evolutionary track corresponding to the best-fit stellar properties (see §6). Because of the large uncertainties in the knowledge of the tidal dissipation in stars and the tidal quality factor,  $Q_*$ , we consider different constant values of the dissipation parameter  $Q'_*$ , namely,  $Q'_* = 10^{6.6}$ ,  $10^7$  and  $10^8$  for KELT-25 and  $Q'_* = 10^5$ ,  $10^6$  and  $10^7$  for KELT-26, where  $Q'_*$  is just proportional to  $Q_*$ . With these assumptions, we proceeded to calculate the past and future evolution of the semi-major axis (in units of the stellar radius) as a function of the age of the system. For KELT-26b, we can see in Figure 16 (Top) that for every assumed dissipation parameter  $Q'_*$ , the planet's orbit moderately decays until the present age of the system. Beyond that point, the future evolution of the planet's orbit strongly depends on  $Q'_*$ : for  $Q'_* = 10^5$ , the planet gradually falls into the star within 500 Myr. For higher values of  $Q'_*$ , the planet would take longer to be engulfed by its host star, perhaps surviving the entire stellar lifetime. As a consequence of its decaying orbit, KELT-26 b's stellar radiation increases for all assumed dissipation parameters, as expected. We further note that KELT-26 b has remained subjected throughout its lifetime to radiation above the  $2 \times 10^8$  ergs $^{-1}$ cm $^{-2}$  insolation threshold established in Demory & Seager (2011). This likely explains why KELT-26 b is presently significantly inflated, with  $R_p = 1.9R_J$ . In contrast to KELT-26, because KELT-25 is so rapidly rotating ( $v \sin I_* = 114.2$  km s $^{-1}$ ) and the stellar rotation period is probably shorter than the companion's orbital period, the object's semi-major axis increases with time, rather than decreases, for all physical values of  $Q'_*$ . The lowest value of  $Q'_*$  of  $10^{6.6}$  predicts the fastest orbital evolution. If  $Q'_*$  is close to  $10^8$ , the decreasing insolation due to the planet's expanding orbit will be offset by an increase in stellar radiation as the evolving host expands, resulting in a net increase in incident flux. For all these calculations, the  $3\sigma$  upper limit on the

mass of KELT-25 b was assumed. Because we did not have the moment of inertia for KELT-25, we could not compute its rotational history, so all the orbital paths were calculated assuming that the spin period of the star has remained constant throughout its lifetime. Assuming that  $Q_*$  is constant, and as long as the orbital period has always remained longer than the stellar spin period, the assumption of a constant rotation does not affect the results. However, if that is not the case, the direction of the evolution would be reversed. Figures 15 and 16 show the semi-major and irradiation evolution of both systems.

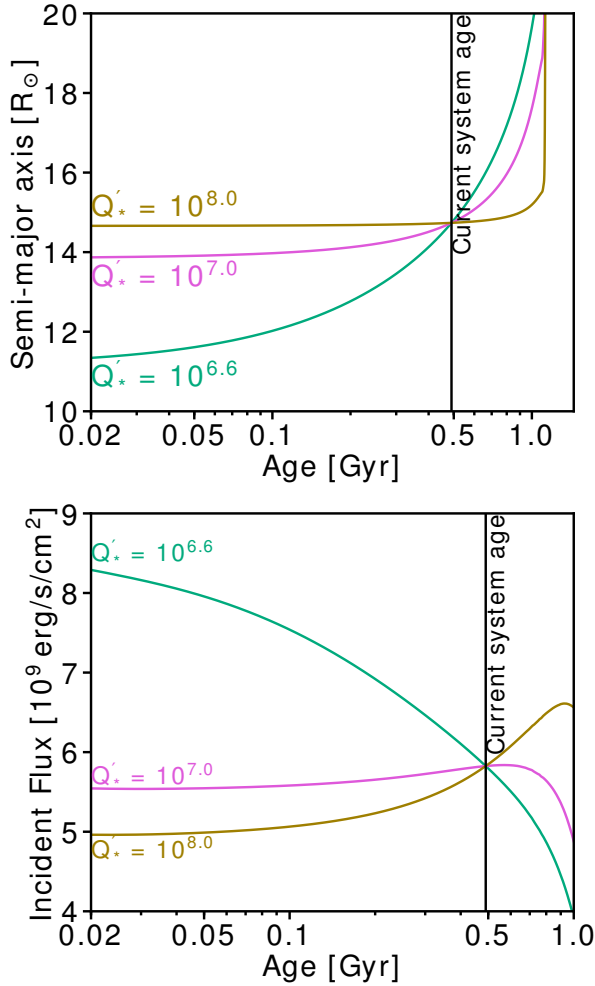


**Figure 15.** Evolution of the semi-major axis in units of stellar radius (**Top**) and incident flux (stellar radiation) as a function of stellar age (**Bottom**) of KELT-25 b for constant values of  $Q_*$  between  $Q_* = 10^{6.6}$  (turquoise line),  $Q_* = 10^7$  (pink) and  $Q_* = 10^8$  (gold). For any given dissipation parameter, the semi-major axis increases with time, while the incident flux decreases.

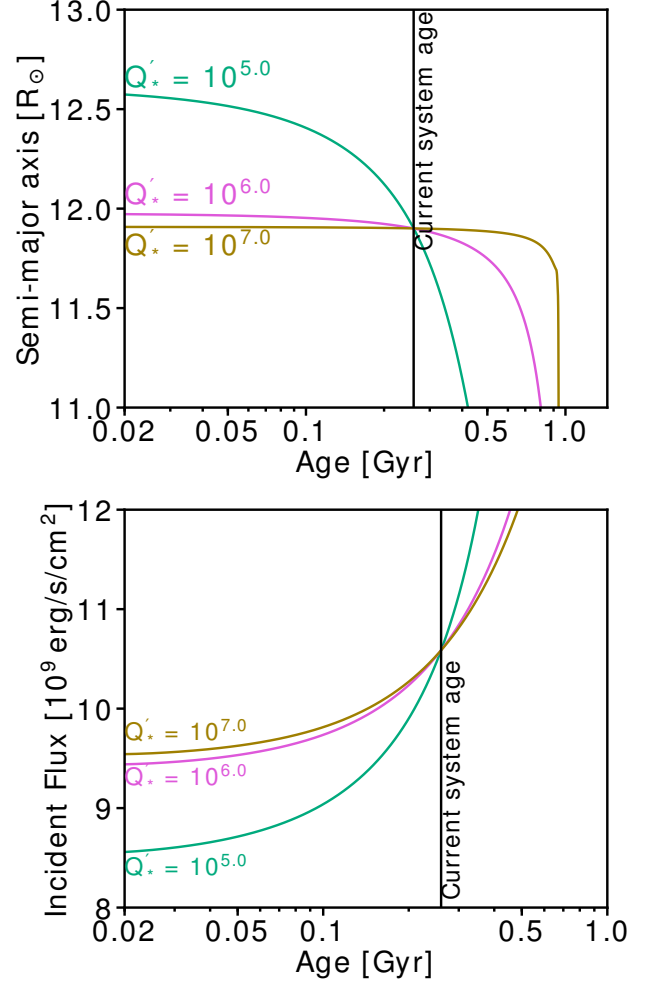


**Figure 16.** Evolution of the semi-major axis in units of stellar radius (**Top**) and incident flux (stellar radiation) as a function of stellar age (**Bottom**) of KELT-26 b for constant values of  $Q_*$  between  $Q_* = 10^5$  (turquoise line),  $Q_* = 10^6$  (pink) and  $Q_* = 10^7$  (gold).

In this paper, we presented the discovery of KELT-25 b, an ultra-hot, sub-stellar companion in a 4.4-day orbit around a young, rapidly-rotating A star; and KELT-26 b, a puffy Ultra Hot Jupiter on a highly inclined, 3.3-day orbit around a young, slowly rotating Am star. Both were also observed by the *TESS* mission. These companions both have exceptionally high equilibrium temperatures and their host stars are bright, making them excellent candidates for follow-up observations. With a rotational velocity of  $v \sin I_* = 114.2 \text{ km s}^{-1}$ , KELT-25 is among the most rapidly rotating A stars with transiting companions, while KELT-26 is in contrast among the slowest. The highly inflated radius of KELT-26 b can provide constraints on empirical mass-radius relations for giant planets. The orbital evolution of KELT-25 b suggests that the semi-major axis is increasing over time, a rather unusual trend for hot Jupiters, which could provide insights



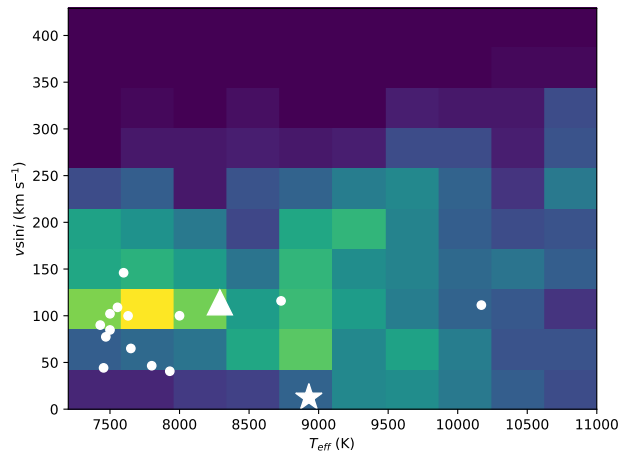


**Figure 17.** Distribution of rotational velocities in units of  $\text{km s}^{-1}$  as a function of stellar effective temperature for all the measured A-type planet hosts in the literature. The color scale is proportional to the fraction of A-stars at that effective temperature that lie within each bin - warmer colors indicate a higher fraction of A-stars. The sample is from Zorec & Royer (2012). The big triangle and star represent KELT-25 and KELT-26, respectively. KELT-26 displays an unusually slow rotation for its temperature, which could be the result of the orientation of its spin-axis along our line of sight rather than an intrinsic slow rotation.

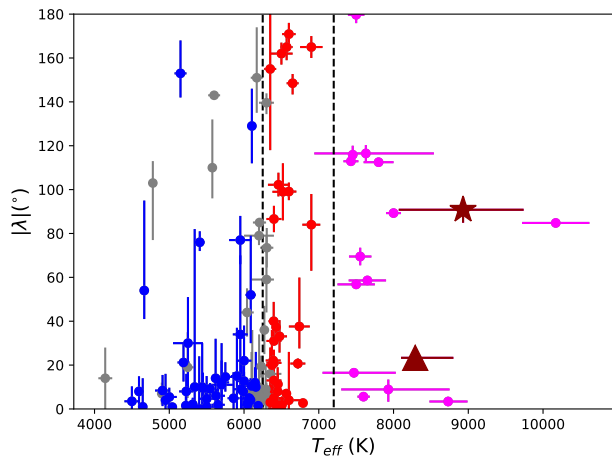


**Figure 18.** Distribution of projected spin-orbit misalignments  $\lambda$  as a function of stellar effective temperature for all the measured hot Jupiters in the literature (the format of this plot is derived from Winn 2010). Planets around cool stars ( $T_{\text{eff}} < 6250$  K) are represented by blue dots; the red dots represent hot stars ( $T_{\text{eff}} > 6250$  K), while those with uncertainties in  $\lambda > 20^\circ$  are colored in gray. The dashed vertical line marks the location of the Kraft break (Left) and the approximate dividing line between F and A spectral types. A-stars are shown in magenta. The crimson star and triangle depict KELT-26 b and KELT-25 b, respectively. The literature sample was taken from John Southworth’s TEPcat Rossiter-McLaughlin catalog<sup>b</sup>

<sup>a</sup><https://www.astro.keele.ac.uk/jkt/tepcat/>

<sup>b</sup><https://www.astro.keele.ac.uk/jkt/tepcat/>

into migration mechanisms for these giant planets. With now roughly a dozen exoplanets detected around A-stars, we begin to have a more comprehensive sample that enables a better understanding of the physical properties, formation and evolution of these systems.

*Software:* EXOFASTv2 (Eastman et al. 2013; ?), AstroImageJ (Collins et al. 2017), SPC (Buchhave et al. 2010)

*Facilities:* FLWO 1.5m (Tillinghast Reflector Echelle Spectrograph, TRES); Kilodegree Extremely Little Telescope (KELT); MINIature Exoplanet Radial Velocity Array (MINERVA); Las Cumbres Observatory at Tenerife (LCO TFN); University of Louisville Manner Telescope (ULMT, Mt. Lemmon); KeplerCam (FLWO 1.2m); Stacja Obserwacji Tranzytów Egzoplanet w Suwałkach (SOTES); CROW Observatory; Koyama Astronomical Observatory (KAO); Gemini-South Zorro

J.E.R. was supported by the Harvard Future Faculty Leaders Postdoctoral fellowship. Work by G.Z. is provided by NASA through Hubble Fellowship grant HST-HF2-51402.001-A awarded by the Space Telescope Science Institute, which is operated by the Association of Universities for Research in Astronomy, Inc., for NASA, under contract NAS 5-26555. D.J.S. is supported by the Penn State University’s Eberly Research Fellowship. The Center for Exoplanets and Habitable Worlds is supported by the Pennsylvania State University, the Eberly College of Science, and the Pennsylvania Space Grant Consortium.

Support for this work was provided by NASA through Hubble Fellowship grant HST-HF2-51399.001 awarded to J.K.T. by the Space Telescope Science Institute, which is operated by the Association of Universities for Research in Astronomy, Inc., for NASA, under contract NAS5-26555.

MNG acknowledges support from MIT’s Kavli Institute as a Juan Carlos Torres Fellow.

C.Z. is supported by a Dunlap Fellowship at the Dunlap Institute for Astronomy & Astrophysics, funded through an endowment established by the Dunlap family and the University of Toronto. K.G.S. acknowledge support from the Vanderbilt Office of the Provost through the Vanderbilt Initiative in Data-intensive Astrophysics. T.N and A.Y. are also grateful to Mizuki Isogai, Akira Arai, and Hideyo Kawakita for their technical support on observations at Koyama Astronomical Observatory. CDK was supported by the Swarthmore College Provost’s Office. This work is partly supported by JSPS KAKENHI Grant Numbers JP18H01265 and JP18H05439, and JST PRESTO Grant Number JP-MJPR1775. J.L.-B. acknowledges support from FAPESP (grant 2017/23731-1). K.P. acknowledges support from NASA grants 80NSSC18K1009 and NNX17AB94G.

Funding for the *TESS* mission is provided by NASA's Science Mission directorate.

This research has made use of the Exoplanet Follow-up Observation Program website, which is operated by the California Institute of Technology, under contract with the National Aeronautics and Space Administration under the Exoplanet Exploration Program.

Resources supporting this work were provided by the NASA High-End Computing (HEC) Program through the NASA Advanced Supercomputing (NAS) Division at Ames Research Center for the production of the SPOC data products.

This paper includes data collected by the *TESS* mission, which are publicly available from the Mikulski Archive for Space Telescopes (MAST)

This work has made use of data from the European Space Agency (ESA) mission *Gaia* (<https://www.cosmos.esa.int/gaia>), processed by the *Gaia* Data Processing and Analysis Consortium (DPAC, <https://www.cosmos.esa.int/web/gaia/dpac/consortium>). Funding for the DPAC has been provided by national institutions, in particular the institutions participating in the *Gaia* Multilateral Agreement. This work makes use of observations from the LCO network. This research has made use of the NASA Exoplanet Archive, which is operated by the California Institute of Technology, under contract with the National Aeronautics and Space Administration under the Exoplanet Exploration Program.

Based on observations obtained at the Gemini Observatory, which is operated by the Association of Universities for Research in Astronomy, Inc., under a cooperative agreement with the NSF on behalf of the Gemini partnership: the National Science Foundation (United States), National Research

Council (Canada), CONICYT (Chile), Ministerio de Ciencia, Tecnología e Innovación Productiva (Argentina), Ministério da Ciência, Tecnologia e Inovação (Brazil), and Korea Astronomy and Space Science Institute (Republic of Korea). Some of the Observations in the paper made use of the High-Resolution Imaging instrument ‘Zorro at Gemini-South). Zorro was funded by the NASA Exoplanet Exploration Program and built at the NASA Ames Research Center by Steve B. Howell, Nic Scott, Elliott P. Horch, and Emmett Quigley.

This research made use of Lightkurve, a Python package for Kepler and TESS data analysis (Lightkurve Collaboration, 2018).

MINERVA-Australis is supported by Australian Research Council LIEF Grant LE160100001, Discovery Grant DP180100972, Mount Cuba Astronomical Foundation, and institutional partners University of Southern Queensland, UNSW Australia, MIT, Nanjing University, George Mason University, University of Louisville, University of California Riverside, University of Florida, and The University of Texas at Austin.

We respectfully acknowledge the traditional custodians of all lands throughout Australia, and recognise their continued cultural and spiritual connection to the land, waterways, cosmos, and community. We pay our deepest respects to all Elders, ancestors and descendants of the Giabal, Jarowair, and Kambuwal nations, upon whose lands the MINERVA-Australis facility at Mt Kent is situated. Resources supporting this work were provided by the NASA High-End Computing (HEC) Program through the NASA Advanced Supercomputing (NAS) Division at Ames Research Center for the production of the SPOC data products.

## REFERENCES

- Addison, B., Wright, D. J., Wittenmyer, R. A., et al. 2019, arXiv e-prints, arXiv:1901.11231
- Alard, C. 2000, *A&AS*, 144, 363
- Alard, C., & Lupton, R. H. 1998, *ApJ*, 503, 325
- Alonso, R., Brown, T. M., Charbonneau, D., et al. 2007, in *Astronomical Society of the Pacific Conference Series*, Vol. 366, *Transiting Extrapolar Planets Workshop*, ed. C. Afonso, D. Weldrake, & T. Henning, 13
- Alsubai, K. A., Parley, N. R., Bramich, D. M., et al. 2011, *MNRAS*, 417, 709
- Anderson, D. R., Temple, L. Y., Nielsen, L. D., et al. 2018, arXiv e-prints, arXiv:1809.04897
- Bakos, G. Á., Kovács, G., Torres, G., et al. 2007, *ApJ*, 670, 826
- Bakos, G. Á., Csubry, Z., Penev, K., et al. 2013, *PASP*, 125, 154
- Barclay, T., Pepper, J., & Quintana, E. V. 2018, *ApJS*, 239, 2
- Barentsen, G., Hedges, C. L., De Miranda Cardoso, J. V., et al. 2019, in *American Astronomical Society Meeting Abstracts*, Vol. 233, *American Astronomical Society Meeting Abstracts #233*, 109.08
- Barnes, J. W. 2009, *ApJ*, 705, 683
- Bayliss, D., Gillen, E., Eig Müller, P., et al. 2018, *MNRAS*, 475, 4467
- Bell, T. J., & Cowan, N. B. 2018, *ApJL*, 857, L20
- Bensby, T., Feltzing, S., & Lundström, I. 2003, *A&A*, 410, 527
- Berta, Z. K., Irwin, J., Charbonneau, D., Burke, C. J., & Falco, E. E. 2012, *AJ*, 144, 145
- Bieryla, A., Collins, K., Beatty, T. G., et al. 2015, *AJ*, 150, 12
- Blake, C. H., Latham, D. W., & Bloom, J. S. 2007, *Astronomical Society of the Pacific Conference Series*, Vol. 366, *The PAIRITEL Ultracool Dwarf Transit Survey*, ed. C. Afonso, D. Weldrake, & T. Henning, 87

- Borucki, W. J., Koch, D., Basri, G., et al. 2010, *Science*, 327, 977
- Bovy, J. 2017, *MNRAS*, 470, 1360
- Brahm, R., Espinoza, N., Jordán, A., et al. 2018, arXiv e-prints, arXiv:1811.02156
- Buchhave, L. A., Bakos, G. Á., Hartman, J. D., et al. 2010, *ApJ*, 720, 1118
- Buchhave, L. A., Latham, D. W., Johansen, A., et al. 2012, *Nature*, 486, 375
- Castelli, F., & Kurucz, R. L. 2003, in *IAU Symposium*, Vol. 210, *Modelling of Stellar Atmospheres*, ed. N. Piskunov, W. W. Weiss, & D. F. Gray, A20
- Cauley, P. W., Shkolnik, E. L., Ilyin, I., et al. 2019, *AJ*, 157, 69
- Charbonneau, D., Brown, T. M., Latham, D. W., & Mayor, M. 2000, *ApJL*, 529, L45
- Charbonneau, D., Berta, Z. K., Irwin, J., et al. 2009, *Nature*, 462, 891
- Choi, J., Dotter, A., Conroy, C., et al. 2016, *ApJ*, 823, 102
- Ciardi, D. R., Beichman, C. A., Horch, E. P., & Howell, S. B. 2015, *ApJ*, 805, 16
- Coşkunoğlu, B., Ak, S., Bilir, S., et al. 2011, *MNRAS*, 412, 1237
- Collier Cameron, A., Pollacco, D., Hellier, C., et al. 2009, in *IAU Symposium*, Vol. 253, *Transiting Planets*, ed. F. Pont, D. Sasselov, & M. J. Holman, 29–35
- Collier Cameron, A., Wilson, D. M., West, R. G., et al. 2007, *MNRAS*, 380, 1230
- Collier Cameron, A., Guenther, E., Smalley, B., et al. 2010a, *MNRAS*, 407, 507
- . 2010b, *MNRAS*, 407, 507
- Collins, K. A., Kielkopf, J. F., Stassun, K. G., & Hessman, F. V. 2017, *AJ*, 153, 77
- Collins, K. A., Collins, K. I., Pepper, J., et al. 2018, *AJ*, 156, 234
- Crane, J. D., Shectman, S. A., Butler, R. P., et al. 2010, *Society of Photo-Optical Instrumentation Engineers (SPIE) Conference Series*, Vol. 7735, *The Carnegie Planet Finder Spectrograph: integration and commissioning*, 773553
- Cutri, R. M., Skrutskie, M. F., van Dyk, S., et al. 2003, *VizieR Online Data Catalog*, 2246, 0
- Dawson, R. I., & Johnson, J. A. 2018, *Annual Review of Astronomy and Astrophysics*, 56, 175
- Dawson, R. I., Murray-Clay, R. A., & Johnson, J. A. 2015, *ApJ*, 798, 66
- Delrez, L., Gillon, M., Queloz, D., et al. 2018, in *Society of Photo-Optical Instrumentation Engineers (SPIE) Conference Series*, Vol. 10700, *Proc. SPIE*, 107001I
- Demory, B.-O., & Seager, S. 2011, *ApJS*, 197, 12
- Dholakia, S., Dholakia, S., Cody, A. M., et al. 2019, *PASP*, 131, 114402
- Donati, J.-F., Semel, M., Carter, B. D., Rees, D. E., & Collier Cameron, A. 1997, *MNRAS*, 291, 658
- Dorval, P., Talens, G. J. J., Otten, G. P. P. L., et al. 2019, arXiv e-prints, arXiv:1904.02733
- Dotter, A. 2016, *ApJS*, 222, 8
- Drake, A. J. 2003, *ApJ*, 589, 1020
- Eastman, J. 2017, EXOFASTv2: Generalized publication-quality exoplanet modeling code, *Astrophysics Source Code Library*, ascl:1710.003
- Eastman, J., Gaudi, B. S., & Agol, E. 2013, *PASP*, 125, 83
- Eastman, J. D., Rodriguez, J. E., Agol, E., et al. 2019, arXiv e-prints, arXiv:1907.09480
- Esteves, L. J., De Mooij, E. J. W., & Jayawardhana, R. 2015, *ApJ*, 804, 150
- Fűrész, G. 2008, PhD thesis, University of Szeged, Hungary
- Gaia Collaboration, Brown, A. G. A., Vallenari, A., et al. 2018, ArXiv e-prints, arXiv:1804.09365
- Gaudi, B. S., & Winn, J. N. 2007, *ApJ*, 655, 550
- Gaudi, B. S., Stassun, K. G., Collins, K. A., et al. 2017, *Nature*, 546, 514
- Gillon, M., Triaud, A. H. M. J., Demory, B.-O., et al. 2017, *Nature*, 542, 456
- Gould, A., & Morgan, C. W. 2003, *ApJ*, 585, 1056
- Gould, A., Pepper, J., & DePoy, D. L. 2003, *ApJ*, 594, 533
- Gravity Collaboration, Abuter, R., Amorim, A., et al. 2019, *A&A*, 625, L10
- Grether, D., & Lineweaver, C. H. 2006, *ApJ*, 640, 1051
- Hartman, J. D., Bakos, G. Á., Buchhave, L. A., et al. 2015, *AJ*, 150, 197
- Hébrard, G., Désert, J. M., Díaz, R. F., et al. 2010, *A&A*, 516, A95
- Hellier, C., Anderson, D. R., Bouchy, F., et al. 2019, *MNRAS*, 482, 1379
- Henry, G. W., Marcy, G. W., Butler, R. P., & Vogt, S. S. 2000, *ApJL*, 529, L41
- Hoeijmakers, H. J., Ehrenreich, D., Kitzmann, D., et al. 2019, *A&A*, 627, A165
- Høg, E., Fabricius, C., Makarov, V. V., et al. 2000, *A&A*, 355, L27
- Howell, S. B., Everett, M. E., Sherry, W., Horch, E., & Ciardi, D. R. 2011, *AJ*, 142, 19
- Howell, S. B., Scott, N. J., Matson, R. A., Horch, E. P., & Stephens, A. 2019, *AJ*, 158, 113
- Jenkins, J. M., Twicken, J. D., McCauliff, S., et al. 2016, in *Proc. SPIE*, Vol. 9913, *Software and Cyberinfrastructure for Astronomy IV*, 99133E
- Johnson, J. A., Fischer, D. A., Marcy, G. W., et al. 2007, *ApJ*, 665, 785
- Johnson, J. A., Clanton, C., Howard, A. W., et al. 2011, *ApJS*, 197, 26
- Johnson, M. C., Cochran, W. D., Albrecht, S., et al. 2014, *ApJ*, 790, 30
- Johnson, M. C., Cochran, W. D., Collier Cameron, A., & Bayliss, D. 2015, *ApJL*, 810, L23

- Johnson, M. C., Rodriguez, J. E., Zhou, G., et al. 2018, *AJ*, 155, 100
- Kitzmann, D., Heng, K., Rimmer, P. B., et al. 2018, *ApJ*, 863, 183
- Kounkel, M., & Covey, K. 2019, *AJ*, 158, 122
- Kovács, G., Zucker, S., & Mazeh, T. 2002, *A&A*, 391, 369
- Kraft, R. P. 1967, *ApJ*, 150, 551
- Kuhn, R. B., Rodriguez, J. E., Collins, K. A., et al. 2016, *MNRAS*, 459, 4281
- Lesage, A. L., Spronck, J. F. P., Stuik, R., et al. 2014, in *Society of Photo-Optical Instrumentation Engineers (SPIE) Conference Series*, Vol. 9145, Proc. SPIE, 914514
- Lightkurve Collaboration, Cardoso, J. V. d. M., Hedges, C., et al. 2018, *Lightkurve: Kepler and TESS time series analysis in Python*, *Astrophysics Source Code Library*, ascl:1812.013
- Loeb, A., & Gaudi, B. S. 2003, *ApJL*, 588, L117
- Lomb, N. R. 1976, *Ap&SS*, 39, 447
- Lothringer, J. D., Barman, T., & Koskinen, T. 2018, *ApJ*, 866, 27
- Lund, M. B., Rodriguez, J. E., Zhou, G., et al. 2017, *AJ*, 154, 194
- Matson, R. A., Howell, S. B., & Ciardi, D. 2018, *arXiv e-prints*, arXiv:1811.02108
- McCullough, P. R., Stys, J. E., Valenti, J. A., et al. 2005, *PASP*, 117, 783
- Murphy, S. J., Hey, D., Van Reeth, T., & Bedding, T. R. 2019, *MNRAS*, 485, 2380
- Nielsen, L. D., Bouchy, F., Turner, O., et al. 2019, *A&A*, 623, A100
- Nutzman, P., & Charbonneau, D. 2008, *PASP*, 120, 317
- Pavlenko, Y. V., Jenkins, J. S., Jones, H. R. A., Ivanyuk, O., & Pinfield, D. J. 2012, *MNRAS*, 422, 542
- Paxton, B., Bildsten, L., Dotter, A., et al. 2011, *ApJS*, 192, 3
- Paxton, B., Cantiello, M., Arras, P., et al. 2013, *ApJS*, 208, 4
- Paxton, B., Marchant, P., Schwab, J., et al. 2015, *ApJS*, 220, 15
- Penev, K., Zhang, M., & Jackson, B. 2014, *PASP*, 126, 553
- Pepper, J., Kuhn, R. B., Siverd, R., James, D., & Stassun, K. 2012, *PASP*, 124, 230
- Pepper, J., Pogge, R. W., DePoy, D. L., et al. 2007, *PASP*, 119, 923
- Pollacco, D. L., Skillen, I., Collier Cameron, A., et al. 2006, *PASP*, 118, 1407
- Quinn, S. N., White, R. J., Latham, D. W., et al. 2012, *ApJL*, 756, L33
- Ricker, G. R., Winn, J. N., Vanderspek, R., et al. 2015, *Journal of Astronomical Telescopes, Instruments, and Systems*, 1, 014003
- Rodriguez, J. E., Quinn, S. N., Huang, C. X., et al. 2019a, *AJ*, 157, 191
- Rodriguez, J. E., Eastman, J. D., Zhou, G., et al. 2019b, *AJ*, 158, 197
- Royer, F., Zorec, J., & Gómez, A. E. 2007, *A&A*, 463, 671
- Scargle, J. D. 1982, *ApJ*, 263, 835
- Schlaufman, K. C. 2010, *ApJ*, 719, 602
- Schlegel, D. J., Finkbeiner, D. P., & Davis, M. 1998, *ApJ*, 500, 525
- Scott, N. J., & Howell, S. B. 2018, in *Society of Photo-Optical Instrumentation Engineers (SPIE) Conference Series*, Vol. 10701, Proc. SPIE, 107010G
- Shporer, A., Jenkins, J. M., Rowe, J. F., et al. 2011, *AJ*, 142, 195
- Siverd, R. J., Beatty, T. G., Pepper, J., et al. 2012, *ApJ*, 761, 123
- Siverd, R. J., Collins, K. A., Zhou, G., et al. 2018, *AJ*, 155, 35
- Stassun, K. G., & Torres, G. 2018a, *ApJ*, 862, 61
- , 2018b, *ApJ*, 862, 61
- Stassun, K. G., Oelkers, R. J., Paegert, M., et al. 2019, *AJ*, 158, 138
- Stephan, A. P., Naoz, S., & Gaudi, B. S. 2018, *AJ*, 156, 128
- Stephan, A. P., Naoz, S., Gaudi, B. S., & Salas, J. M. 2019, *arXiv e-prints*, arXiv:1909.05259
- Talens, G. J. J., Albrecht, S., Spronck, J. F. P., et al. 2017, *A&A*, 606, A73
- Talens, G. J. J., Justesen, A. B., Albrecht, S., et al. 2018, *A&A*, 612, A57
- Tokovinin, A. 2018, *PASP*, 130, 035002
- Tokovinin, A., Fischer, D. A., Bonati, M., et al. 2013, *PASP*, 125, 1336
- Winn, J. N. 2010, *Exoplanet Transits and Occultations*, ed. S. Seager, 55–77
- Wong, I., Shporer, A., Morris, B. M., et al. 2019, *arXiv e-prints*, arXiv:1910.01607
- Zacharias, N., Finch, C., & Frouard, J. 2017, *VizieR Online Data Catalog*, 1340
- Zacharias, N., Finch, C. T., Girard, T. M., et al. 2013, *AJ*, 145, 44
- Zhou, G., Rodriguez, J. E., Collins, K. A., et al. 2016, *AJ*, 152, 136
- Zhou, G., Bakos, G. Á., Bayliss, D., et al. 2019a, *AJ*, 157, 31
- Zhou, G., Huang, C. X., Bakos, G. Á., et al. 2019b, *arXiv e-prints*, arXiv:1906.00462
- Ziegler, C., Tokovinin, A., Briceno, C., et al. 2019, *arXiv e-prints*, arXiv:1908.10871
- Zorec, J., & Royer, F. 2012, *A&A*, 537, A120